cVl__chemgreek_uppercase_mapping_2_prop1l__chemgreek_lowercase_mapping_2_prop1l__chemgreek_
l__chemgreek_lowercase_mapping_1_prop1l__chemgreek_uppercase_mapping_1_prop1

Brown and black carbon emitted by a marine engine operated on heavy fuel oil and distillate fuels: optical properties, size distributions, emission factors

J. C. Corbin*[1], S. M. Pieber[1], H. Czech[2], M. Zanatta[1], G. Jakobi[3,4], D. Massabò[5,6], J. Orasche[2,3,4], I. El Haddad[1], A. A. Mensah[7], B. Stengel[4,8], L. Drinovec[9,10], G. Močnik[9,10], R. Zimmermann[2,3,4], A. S. H. Prévôt[1], M. Gysel[1]**

[1]Laboratory of Atmospheric Chemistry, Paul Scherrer Institute, CH-6232 Villigen, Switzerland
[2]Joint Mass Spectrometry Centre, Chair of Analytical Chemistry, Institute of Chemistry, University of Rostock, Dr.-Lorenz-Weg 1, 190610 Rostock, Germany
[3]Joint Mass Spectrometry Centre, Cooperation Group Comprehensive Molecular Analytics, Helmholtz Zentrum München, Ingolstädter Landstr. 1, 96875 Neuherberg, Germany
[4]HICE – Helmholtz Virtual Institute for Complex Molecular Systems in Environmental Health, Germany
[5]Department of Physics, University of Genoa, Via Dodecaneso 33, 17157 Genova, Italy
[6]INFN, Sezione di Genova, Via Dodecaneso 22, 17157 Genova, Italy
[7]Institute for Atmospheric and Climate Science, ETH Zurich, 90102 Zurich, Switzerland
[8]Department of Piston Machines and Internal Combustion Engines, University of Rostock, Albert-Einstein-Str. 2, 190610 Rostock, Germany
[9]Aerosol d.o.o., 1000 Ljubljana, Slovenia
[10]Condensed Matter Physics Department, Jožef Stefan Institute, Ljubljana, Slovenia
*Now at: National Research Council Canada, Ottawa, Canada
**Now at: Alfred Wegener Institute, Bussestrasse 27, 27570 Bremerhaven, Germany

Key Points:

- 50 % and 20 % of light absorption at 370 nm and 590 nm, respectively, was due to "brown carbon" in the exhaust of an engine operated on heavy fuel oil (HFO).
- HFO contains very large rBC particles (mode at 640 nm rBC-volume-equivalent diameter).
- HFO-brown-carbon λ-dependent imaginary refractive indices and mass absorption cross-sections are much higher than previously estimated.

Corresponding author: Martin Gysel, martin.gysel@psi.ch

Abstract

We characterized the chemical composition and optical properties of particulate matter (PM) emitted by a marine diesel engine operated on heavy fuel oil (HFO), marine gas oil (MGO) and diesel fuel (DF). For all three fuels, $\sim$ 80% of submicron PM was organic (and sulfate, for HFO at higher engine loads). Emission factors varied only slightly with engine load. Refractory black carbon (rBC) particles were not thickly coated for any fuel; rBC was therefore externally mixed from organic and sulfate PM. For MGO and DF PM, rBC particles were lognormally distributed in size (mode at $d_{\mathrm{rBC}} \approx 120\,\mathrm{nm}$). For HFO, much larger rBC particles were present. Combining the rBC mass concentrations with in-situ absorption measurements yielded an rBC mass absorption coefficient $\mathrm{MAC}_{\mathrm{BC},780\,\mathrm{nm}}$ of $7.8 \pm 1.8\,\mathrm{m^2\,g^{-1}}$ at 780 nm for all three fuels. Using positive deviations of the absorption Ångström exponent (AAE) from unity to define brown carbon (brC), we found that brC absorption was negligible for MGO or DF PM ($\mathrm{AAE}(370,880\,\mathrm{nm}) \approx 1.0 \pm 0.1$) but typically 50 % of total 370 nm absorption for HFO PM. Even at 590 nm, $\sim$ 20 % of the total absorption was due to brC. Using absorption at 880 nm as a reference for BC absorption and normalizing to organic PM mass, we obtained a $\mathrm{MAC}_{\mathrm{OM},370\,\mathrm{nm}}$ of $0.4\,\mathrm{m^2\,g^{-1}}$ at typical operating conditions. Furthermore, we calculated an imaginary refractive index of $(0.045 \pm 0.025)(\lambda/370\,\mathrm{nm})^{-3}$ for HFO PM at $370\,\mathrm{nm} > \lambda > 660\,\mathrm{nm}$, more than twofold greater than previous recommendations. Climate models should account for this substantial brC absorption in HFO PM.

Plain language summary (JGR feature)

We characterized the fundamental properties of marine-engine exhaust that are relevant to its aerosol-radiation interactions in climate models. In particular, we focussed on "brown carbon" light absorption (i.e., absorption in excess of that expected for the black carbon in canonical soot). We found that brown carbon can increase the 370 nm direct radiative forcing of heavy-fuel-oil marine exhaust by 18 % over snow.

1 Introduction

Ship engines are the major source of combustion aerosols in the marine environment, where almost no other anthropogenic pollution sources exist. Understanding the climate-relevant optical properties of this particulate matter (PM) is therefore essential to the accurate determination of anthropogenic radiative effects on the marine atmosphere [*Endresen*, 2003; *Lauer et al.*, 2007; *Unger et al.*, 2010; *Lindstad et al.*, 2015; *Marelle et al.*, 2016]. In addition, a large fraction of ship PM is emitted near shore [*Eyring et al.*, 2010], which has a strong potential to negatively impact human health [*Corbett et al.*, 2007; *Oeder et al.*, 2015] as well as visibility.

Ship-engine PM contains significant amounts of organic PM (OM) as well as black carbon (BC) [*Lack et al.*, 2009; *Buffaloe et al.*, 2014; *Mueller et al.*, 2015; *Price et al.*, 2016]. When heavy fuel oil (HFO) is used, sulfates also contribute significantly to PM

mass [*Lack et al.*, 2009; *Popovicheva et al.*, 2009; *Mueller et al.*, 2015]. Typically, BC contributes a relatively small fraction to the mass of HFO PM. The overall single-scattering albedo (SSA) of HFO PM aerosols is therefore relatively high, such that ship-engine PM may result in an overall cooling over the (low-albedo) ocean surface [*Lauer et al.*, 2007; *Unger et al.*, 2010], but a localized warming over high-albedo surfaces or on snow and ice [*Lack and Corbett*, 2012]. The accurate quantification of these radiative effects requires an accurate measurement of the light-absorption properties of both BC and OM.

Light-absorbing OM has previously been inferred to contribute significantly to total HFO PM absorption at shorter visible wavelengths λ, based on the observation of 2-λ absorption Ångström exponents (AAE(370, 880 nm); Eq. 1) much greater than unity [*Mueller et al.*, 2015]. Accounting for this light-absorbing OM in radiative models of the Earth's atmosphere requires knowledge of intensive optical properties, such as imaginary refractive index (k_{OM}) and mass absorption cross-section ($\mathrm{MAC}_{\mathrm{OM}}$), which have not previously been reported.

A major goal of the present work was to quantify k_{OM} and $\mathrm{MAC}_{\mathrm{OM}}$ for use in climate models. This quantification was achieved by applying the popular [*Fialho et al.*, 2005; *Sandradewi et al.*, 2008; *Favez et al.*, 2009; *Grenfell et al.*, 2011; *Bahadur et al.*, 2012; *Cazorla et al.*, 2013; *Lack and Langridge*, 2013; *Yuan et al.*, 2016; *Pokhrel et al.*, 2017; *Zotter et al.*, 2017] two-component "BC+brC" model: (i) light absorption in the near infrared ($\lambda \geq 780$ nm) is attributed to BC only, (ii) BC absorption is assumed to depend inversely on λ ($\mathrm{AAE}_{\mathrm{BC}} = 1$), and (iii) when measured visible-light absorption exceeds predicted absorption by BC, the excess is attributed to light-absorbing OM (so-called brown carbon or brC). In this context, we define BC as refractory, light-absorbing carbon with an AAE of unity between 370 nm $< \lambda <$ 950 nm [*Petzold et al.*, 2013]. We consider BC as the sole light-absorbing species at $\lambda \geq 780$ nm and, when the aerosol AAE exceeds unity, attribute the excess absorption to brC. While brC is therefore defined purely from the optical properties of the aerosol, we also calculate intensive brC properties by normalizing brC absorption to total organic PM mass.

For HFO PM, the two-component BC+brC absorption approach may not fully describe the aerosol. First, HFO exhaust may contain asphaltenes, large polyaromatic molecules that may contribute to PM light absorption in the near infrared, besides BC [*Mullins*, 2010]. Second, light-absorbing char particles may also be present in HFO PM [*Lyyränen et al.*, 1999; *Chen et al.*, 2005; *Popovicheva et al.*, 2009]. These char particles are formed when fuel droplets graphitize rather than vapourize at the high flame temperatures [*Linak et al.*, 2000] and are therefore a subcategory of BC, with typical physical diameters of $\sim 1\,\mu$m. Their large physical diameter places char particles outside of the Rayleigh regime, potentially invalidating the $\mathrm{AAE}_{\mathrm{BC}} = 1$ assumption of the BC+brC approach. Unfortunately, our present measurements do not provide sufficient information to address these char particles explicitly. To the extent that $\mathrm{AAE}_{\mathrm{char}} \neq 1$, our approach may overestimate or underestimate the absorption properties of brC. However, even if this was the case, our two-species (BC+brC) approach would still provide the optical parameters re-

quired for climate models to correctly represent the wavelength-dependent light absorption of HFO PM which we have observed; the inaccuracy would be in the relative attribution of absorption to the different light-absorbing species. Moreover, as demonstrated by *Saleh et al.* [2016], climate models which employ Mie theory in radiative transfer calculations produce more accurate estimates of radiative forcing when Mie-theory-retrieved parameters are used, compared to more-complex retrievals.

In the following, we determine the optical properties of brC from a ship engine operating on three different fuels: HFO, marine gas oil (MGO), and EN 590 diesel fuel (DF). The upcoming sections discuss (1) speciated PM emission factors and the PM mixing state, (2) the PM SSA and MAC_{BC} at 780 nm obtained by the extinction-minus-scattering technique combined with refractory BC (rBC) mass concentrations measured by a single particle soot photometer (SP2) and (3) brC absorption using the BC+brC conceptual model in terms of MAC_{OM} and k_{OM} by using OM concentrations measured by an aerosol mass spectrometer (AMS). Note that the analysis in part (3) does not incorporate the SP2 measurements.

2 Methods

2.1 Experimental

The engine used in this study was a single-cylinder research engine installed at the Institute of Piston Machines and Internal Combustion Engines at the University of Rostock in Germany. The size of the combustion chamber and layout of the engine is typical of engines used on smaller ships as a main power supply, on large ships for ancillary power, or as a backup power supply on land, e.g. in hospitals. The engine is of a four-stroke, single-cylinder design, with a 150 mm bore and 180 mm stroke and operates at a nominal 1500 rpm with a maximum power of 80 kW. Previous publications have provided further details on the engine [*Oeder et al.*, 2015; *Streibel et al.*, 2017] and reported detailed characterizations of its emissions [*Mueller et al.*, 2015], however, we emphasize that the engine was reconfigured between these two studies. During this study, certain engine operating parameters were varied to investigate their influence on the emissions; none of these parameters were identified as having influenced the properties discussed herein. The measurements took place between November 10th and December 9th, 2014.

The sampling system was similar to that used by *Streibel et al.* [2017] and is shown in Fig. 1. Emissions (sampled 1.5 m from the engine at $> 500\,^{\circ}C$) were first passed through 300 °C heated lines to a pre-cyclone with a nominal cut-off aerodynamic diameter of 2.5 μm, then diluted by a factor of roughly 12 in a two-stage dilutor. The two-stage dilutor combined a porous-tube stage, where compressed air flowed through pores in a cylinder to provide a sheath flow and minimize wall losses, with an ejector dilutor, at a flow rate of 150 L min^{-1}. The exact dilution ratio was measured by online CO_2 monitors. After this dilution stage, filter samples for thermal/optical reflectance analysis (resulting in NIOSH 5040 EC/OC data) and elemental analysis (discussed elsewhere; *Corbin et al.* 2017) were

taken. Subsequently, two tenfold ejector dilutors (Dekati Ltd., Finland) were employed to reduce PM concentrations to atmospheric levels and ambient temperatures. The steel sampling line (10 mm i.d.) to the aethalometer was approximately 5 m long with a total flow of 4.5 $\mathrm{L\,min^{-1}}$, while the other online instruments sampled at a total of 13 $\mathrm{L\,min^{-1}}$ through first ~7 m section of tubing and then at 3 $\mathrm{L\,min^{-1}}$ through a second 3 m section of tubing. This flow was then divided between similar lengths of line for the instruments.

The majority of the instruments sampled at high time resolution (1 min or faster), with the exception of the particle-filter samples. For the data presented below, the 30 minute filter samples were generally used to define periods of interest (after manual inspection) and data were averaged over these periods.

Particle size distributions were obtained by a Scanning Mobility Particle Sizer (SMPS; ^{85}Kr bipolar charger; PSI-constructed DMA equivalent to the model 3081 of TSI Inc., USA; TSI CPC 3022A) and Fast Mobility Particle Sizer (FMPS, model 3091, TSI Inc.). The SMPS measurements are considered more reliable as data-inversion issues (influencing both sizing and counting) have been reported for the FMPS [*Zimmerman et al.*, 2015]. We therefore used the SMPS data to obtain geometric standard deviations (GSD) of the size distribution for the Mie model. However, due to limited coverage of these SMPS data, the FMPS data were used to obtain geometric mean particle diameters (GMDs). These were retrieved from the FMPS data by fitting a bimodal lognormal function to the data using custom code written in Igor Pro (version 6.32, WaveMetrics, OR, USA). The FPMS data were first corrected using the routine published by *Zimmerman et al.* [2015], which uses a separate CPC 3022A as a reference for the overall number concentration. The GMD obtained from the corrected FMPS data is considered more reliable than the FMPS GSD [*Zimmerman et al.*, 2015].

For some samples, aerosol particle mass was measured for mobility-size-selected particles using a home-built DMA and a CPC (Model 3022A, TSI Inc. USA) sampling behind an Aerosol Particle Mass analyzer (APM Model 3601, Kanomax Japan). The DMA-APM-CPC data was analyzed as described in *Zieger et al.* [2017] to yield particle effective density measurements for the ultrafine mode, which was dominated by organics and sulfate. Considering that the organic–sulfate ultrafine particles were liquid and therefore spherical, these effective densities correspond directly to particle densities. Effective density measurements of rBC were attempted, but were not feasible as the rBC number concentrations were much lower.

2.2 Single Particle Soot Photometer (SP2)

A Single Particle Soot Photometer (SP2; Droplet Measurement Technologies, CO, USA) was employed to measure black carbon concentrations by laser-induced incandescence [*Stephens et al.*, 2003; *Schwarz et al.*, 2006]. Data were analyzed using the PSI SP2 Toolkit, version 4.112. The SP2 brings BC-containing particles to incandescence during their passage through a continuous-wave, intracavity, 1064 nm laser. The instrument detects rBC cores with mass (or volume-equivalent size, d_{rBC}, considering a void-free mate-

rial density of 1800 kg m^3) from ~ 0.7 fg (~ 80 nm) to ~ 200 fg (~ 600 nm). For particles in this size range, the total rBC mass reported by SP2 has been validated as accurate by multiple independent studies *Slowik et al.* [2007]; *Kondo et al.* [2011]; *Laborde et al.* [2012a]. The total mass concentration reported below is corrected for the mass fraction outside of this range (Section 3.1.1). We use the term "rBC" as recommended by *Petzold et al.* [2013] whenever reporting SP2 data in a quantitative manner, e.g. C_{rBC} for BC mass concentrations and d_{rBC} for mass-equivalent diameters. We use the term rBC core to clarify that any non-refractory, internally-mixed material is not measured by incandescence as it vaporizes well below the ~4000 K sublimation point of BC.

The SP2 also collects light-scattering signals, acting as an optical sizer for BC-free particles ($d_{\mathrm{minimum}} \approx 160$ nm). For BC-containing particles, the scattering signal requires careful data processing because laser heating causes coatings to evaporate during measurement. This evaporation is observable in the time-resolved scattering signals. For uncoated or moderately-coated particles, peak scattering signals occur when particles are relatively closer to the centre of the Gaussian profile of the SP2 laser (since incident light intensity is highest closer to the centre) and simultaneously with particle incandescence. For thickly coated particles, this peak is observed substantially earlier and prior to particle incandescence, corresponding to the substantial reduction in particle volume when coating material evaporates. This binary mixing-state classification is commonly referred to as "delay-time analysis" [*Moteki and Kondo*, 2007]. On this basis, particles can be classified as either 'thickly-coated' (significant difference between peak scattering and incandescence signals) or 'moderately- or uncoated' (no significant difference). The lower detection limit for this classification is higher than that for rBC quantification, since the SP2 scattering measurement is less sensitive than the incandescence measurement. The upper limit for this classification is imposed by saturation of the scattering signal detector, which occurs for large overall particle sizes. We present data only for particles within these limits. Note that a particle consisting of an rBC particle coagulated with other material may appear to be 'thickly-coated' in the SP2, resulting in an overestimated fraction of thickly-coated particles. Note also that a precise distinction between 'moderate or no coating' and 'thick coating', for example in terms of BC volume fraction, cannot be given without knowledge of the thermochemical properties of the coating [*Sedlacek et al.*, 2015]. Based on our previous comparisons of coating-thickness to delay-time data for atmospheric BC particles (unpublished work), we estimate that 'moderate or no coating' describe particles containing 70–100 % rBC volume.

A more complex data analysis approach allows the coating thickness of BC-containing particles to be retrieved quantitatively, as follows. By retrieving the scattering signal at 3 % of the maximum laser intensity, at which point no coating material has yet evaporated, the scattering cross-section of the total, possibly-coated, particle can be determined [*Gao et al.*, 2007; *Taylor et al.*, 2015]. Conversely, by retrieving the scattering signal after coatings have evaporated but before the onset of incandescence, the scattering cross-section of uncoated rBC can be determined [*Laborde et al.*, 2012b]. The latter value can be used to calculate the rBC-mass-equivalent volume of the rBC core, given a com-

plex refractive index of the core $m_{\mathrm{core}} = (n, k)$. The precise value of m_{core} is not well constrained and may vary between BC materials, but the empirical relationship $k \approx (n-1)$ has been shown by *Bond and Bergstrom* [2006], as discussed further by *Moteki et al.* [2010]. Employing this constraint, we determined m_{core} as $1.9{+}0.8i$ by fitting the rBC-core volume determined by scattering to that determined by incandescence. Our approach of adjusting m_{core} only serves as an internal calibration of the coating-thickness retrieval, and must not be misinterpreted as a measurement of the BC refractive index, which would require additional independent measurements. Our value of m_{core} is smaller than that typically used in SP2 analysis ($2.26 + 1.26i$), but is consistent with that used by *Laborde et al.* [2012a] for propane-flame soot. Using the typical m_{core} value of $2.26 + 1.26i$ corresponds to smaller rather than larger coating thicknesses in the analysis presented below. We note that it is typical to observe some negative coating thicknesses in this analysis due to random noise on the single-particle level. Investigations in our laboratory have found that this noise is due mainly to the variability of particle velocity through the laser beam and uncertainty in determining the scattering signal at 3 % of the maximum laser intensity. The retrieval of the scattering signal at 3 % of the maximum laser intensity means that the lower detection limit for coating-thickness analysis is substantially higher than for delay-time analysis.

The SP2 was operated and calibrated as described in [*Laborde et al.*, 2012a]. Briefly, mass-selected rBC particles representative of atmospheric or diesel rBC (Alfa Aeser Inc., FS, Lot #FS12S011) were used to calibrate the peak incandescence signal and polystyrene latex (PSL) sphere standards of diameter 269 nm were used to calibrate the partial scattering cross section measurements.

2.3 Aerosol Mass Spectrometer (AMS)

Particles are introduced into the High-ResolutionAerosol Mass Spectrometer (AMS) by an aerodynamic lens [*Liu et al.*, 2007] which has its maximum transmission efficiency between about 100 nm to 600 nm in free-molecular aerodynamic diameter ($d_{\mathrm{fm,a}}$). Note that this aerodynamic diameter is weighted by particle density [*Kulkarni et al.*, 2011], so that $d_{\mathrm{fm,a}} = 100$ nm corresponds to a volume-equivalent diameter of 69 nm for the HFO PM density reported below. Non-refractory material in these particles is then vaporized by an 873 K porous-tungsten cone before electron ionization. The resulting ions are analyzed in a high-resolution time-of-flight mass spectrometer [*DeCarlo et al.*, 2006]. Note that we have used the term "sulfate" below rather than "sulfuric acid" (the likely form of sulfate, as discussed below) because sulfate and nitrate are the chemical components measured by AMS after electron ionization. For a more detailed discussion of the AMS results of this study, see *Corbin et al.* [2017].

2.4 Optical measurements

The aerosol absorption coefficient was measured by the extinction-minus-scattering technique, using a Cavity Attenuation Phase Shift PM SSA monitor [CAPS PMssa, *Onasch et al.*, 2015] operating at 780 nm. This instrument provides a calibration-free measure of

extinction (manufacturer-estimated accuracy: 5 %). The extinction measurement occurs in an optical cell surrounded by an integrating-sphere nephelometer. This nephelometer was calibrated using the extinction measurement, as described in *Onasch et al.* [2015], using 269 nm diameter polystyrene latex spheres and size-selected NH_4NO_3. We also performed a calibration at the Paul Scherrer Institute using pure N_2 and CO_2. Overall, eight calibrations over 13 months using all of these approaches showed a relative standard deviation of only 10%, indicating very stable instrument performance. Data were manually inspected to ensure that baseline values of extinction and scattering (obtained periodically on filtered samples) were stable. Note that during engine measurements, the CAPS PMssa was occasionally diluted by a factor of 5.1 owing to flow limitations in some experiments (not presented here), which was tested and found to have no effect on the resulting data.

Some data were also acquired using CAPS PMssa instruments operating at 450 nm and 630 nm. These data are not presented here due to issues with data quality, possibly due to the difficulty of obtaining a valid baseline measurement when variable amounts of absorbing gases with strong surface interactions, such as NO_2, are present.

An aethalometer (model AE33, Aerosol d.o.o., Slovenia) was also deployed during these experiments. The AE33 measures the light attenuation through a PM deposit on a filter at seven wavelengths λ. The AE33 converts filter-deposit attenuation coefficients to aerosol light absorption coefficients by applying a conversion factor (known as the "C value") as detailed in *Drinovec et al.* [2015] and discussed further in Section S3, where the calibration factor is evaluated for our samples at 780 nm. To avoid issues due to pressure changes in the sampling lines due to changes in engine conditions, our AE33 data was reanalyzed with a constant compensation parameter [defined in *Drinovec et al.*, 2015].

Three filter samples were also measured with the Multi-Wavelength Absorbance Analyzer [MWAA; *Massabò et al.*, 2013, 2015] with the goal of evaluating the performance of the CAPS PMssa. In particular, the wavelength dependence of the aethalometer calibration could be confirmed as negligible using the MWAA data. This is evident in Fig. 6, as discussed further in the supplement.

2.5 Optical calculations

Using the AE33 data, the AAE was calculated as the two-wavelength AAE:

$$\mathrm{AAE}(\lambda_1, \lambda_2) = -\frac{\ln\left(b_{\mathrm{ATN},\lambda_1}/b_{\mathrm{ATN},\lambda_2}\right)}{\ln\left(\lambda_1/\lambda_2\right)} \tag{1}$$

where the subscripts 1 and 2 indicate two different measurement wavelengths, λ is a measurement wavelength, and $b_{\mathrm{ATN},\lambda}$ is an AE33-measured attenuation coefficient.

Using the CAPS PMssa data, $b_{\mathrm{abn},\lambda}$ was calculated at λ =780 nm by subtracting the measured scattering from the measured extinction coefficient. By combining the CAPS PMssa $b_{\mathrm{abn},780}$ with the measured AAEs, we also calculated $b_{\mathrm{abn},\lambda}$ at $\lambda = (370, 470, 520, 590, 660)$ nm.

This calculation is numerically equivalent to calibrating the aethalometer using the CAPS PMssa (full details are given in the supplement). For some samples, CAPS PMssa data were not available for this calibration, and the median C-value from the other calibrations was applied.

The MAC of a species X at a wavelength λ, $\mathrm{MAC}_{X,\lambda}$, was calculated as

$$\mathrm{MAC}_{X,\lambda} = b_{\mathrm{abn},X,\lambda}/C_X, \tag{2}$$

where $b_{\mathrm{abn},X,\lambda}$ is the aerosol absorption coefficient corresponding to absorption by species X. In general, brC is considered to absorb negligibly at longer wavelengths [*Laskin et al.*, 2015], so that we attribute all absorption at $\lambda \geq 780\,\mathrm{nm}$ to BC ($b_{\mathrm{abn,BC},\lambda} \approx b_{\mathrm{abn},\lambda}$) and the equation becomes

$$\mathrm{MAC}_{\mathrm{rBC},780} = b_{\mathrm{abn,BC},780}/C_{\mathrm{rBC}} \approx b_{\mathrm{abn},780}/C_{\mathrm{rBC}}, \tag{3}$$

for BC, with C_{rBC} measured by the SP2, corrected for the mass fraction outside of the SP2 sensitivity range (Section 3.1.1).

Light absorption was attributed to brC when the measured absorption exceeded that predicted by extrapolating measurements at longer wavelengths ($\lambda \geq 780\,\mathrm{nm}$) to shorter ones ($\lambda \leq 660\,\mathrm{nm}$) using an AAE= 1. That is, brC absorption was defined by

$$b_{\mathrm{abn,brC},\lambda} = b_{\mathrm{abn},\lambda} - b_{\mathrm{abn,BC},880}\left(\frac{\lambda}{880\,\mathrm{nm}}\right)^{-\mathrm{AAE,BC}}, \tag{4}$$

where λ and 880 nm represent two measurement wavelengths in nm and the subtracted quantity is the AAE-based estimate of BC absorption at λ, using $\mathrm{AAE_{BC}}= 1$ except during sensitivity tests (see below). Eq. 4 results in a positive value of $b_{\mathrm{abn,brC},\lambda}$ when $\mathrm{AAE_{PM}} > 1$ and zero $b_{\mathrm{abn,brC},\lambda}$ when $\mathrm{AAE_{PM}}= 1$. In no case was $\mathrm{AAE_{PM}} < 1$. While both $b_{\mathrm{abn},\lambda}$ and the AAE may be affected by substantial internal mixing [*Lack and Cappa*, 2010], we expect this effect to be negligible in our data because substantial internal mixing of brC and BC was ruled out by our measurements (Section 3.1.2). Eq. 4 was employed to calculate $b_{\mathrm{abn,brC},\lambda}$ at $\lambda = \{370, 470, 520, 590, 660\}$ nm, corresponding to each wavelength shorter than the reference (CAPS PMssa) $\lambda = 780\,\mathrm{nm}$.

As shown in Eq. 4, we generally used $\lambda_2 = 880\,\mathrm{nm}$ as the reference wavelength. A sensitivity test using $\lambda_2 = 950\,\mathrm{nm}$ changed the calculated brC absorption by HFO by only $< 2\,\%$ on average. (HFO was the only fuel with $\mathrm{AAE_{PM}}$ substantially higher than unity.) Uncertainties in the use of Eq. 4 are discussed in Section 2.7.

The MAC of brC was calculated using Eq. 2 with $b_{\mathrm{abn,brC},\lambda}$ and C_{OM} substituted for $b_{\mathrm{abn},X,\lambda}$ and C_X, respectively:

$$\mathrm{MAC}_{\mathrm{OM},\lambda} = b_{\mathrm{abn,brC},\lambda}/C_{\mathrm{OM}}, \tag{5}$$

where C_{OM} is the OM mass concentration measured by the AMS.

2.6 Mie model

A Mie model was constructed and fitted to the brC absorption and OM mass concentration measurements to obtain imaginary refractive indices of OM, k_{OM}. The model structure, inputs and outputs are depicted in Fig. 2 and described in the following.

As described below, our measurements indicated that these ship-engine emissions can be appropriately modelled as an external mixture of two modes, a larger rBC mode and a smaller nucleation mode (internally mixed OM and sulfate). In estimating $b_{\mathrm{abn,brC},\lambda}$ from Eq. 4, we have already subtracted light absorption by BC from the total, and must only model the brC absorption when fitting the Mie model.

The model therefore consisted of a single lognormal distribution of internally-mixed sulfates and OM; the reported k_{OM} values were obtained by minimizing the difference between the measured absorption and the Mie-predicted absorption of this distribution (each reported k_{OM} was fitted independently of the others). The Mie calculations required several additional pieces of information, which were constrained as follows. The GMD was obtained from bimodal lognormal fits to the FMPS measurements and a GSD of 1.65 was obtained from the SMPS data as described in Section 2.1. The respective fractions of OM and sulfate in the particles were obtained from the AMS data. The particle material density was obtained from the DMA–APM measurements described above. For HFO and MGO PM, the respectively measured material densities were $1460 \pm 50\,\mathrm{kg\,m^{-3}}$ and $900 \pm 40\,\mathrm{kg\,m^{-3}}$. The higher density for HFO PM is due to the presence of sulfate. The density measurements of MGO PM were also used to estimate the density of the DF PM, which was not measured. The measured densities are in good agreement with the density estimated from the mass spectra of these samples [*Kuwata et al.*, 2012], as described in the supplement.

The real refractive index of OM, n_{OM} was taken as $n = 1.5$ [*Lu et al.*, 2015]; the fitted results did not change when varying this value as $n_{\mathrm{OM}} \pm 0.1$. The corresponding $n_{\mathrm{SO_4^{2-}}}$ was taken as 1.35 (sulfuric acid). The overall refractive index of the particles was obtained by combining n_{OM} and $n_{\mathrm{SO_4^{2-}}}$ according to their AMS-measured volume ratios, following the volume-weighted linear mixing rule validated by *Abo Riziq et al.* [2007]. Sensitivity tests indicated that the most sensitive input parameter in this model was the GMD: a large change in GMD of 20 nm corresponded to a change of only ± 0.001 in k_{OM} (k_{OM} was greater than 0.01 for all HFO samples, as shown in Fig. 8 below). Varying other parameters by large amounts (relative to their anticipated uncertainties) generally led

to $< 10\,\%$ change in k_{OM}. We note that the PM density used here was well-constrained by the APM measurements.

Overall uncertainties in k_{OM} were calculated by propagating the numerical uncertainties given below in a Monte Carlo calculation.

2.7 Statistical uncertainties

Unless specified otherwise in this section, uncertainties are statistical imprecisions and are reported as the standard error of the mean ($\sigma_{\bar{x}} = SD/\sqrt{(N)}$, SD = standard deviation) with the averaging periods defined by the 30 minute filter periods mentioned above. For derived quantities, uncertainties were propagated from these $\sigma_{\bar{x}}$.

In the special cases where uncertainties other than statistical noise were known to be significant, those uncertainties were added in quadrature (i.e., possible covariance between these different uncertainties was not addressed):

- For the CAPS PMssa, uncertainties in b_{abn} were propagated from an estimated 5 % accuracy in b_{ext} [as estimated by *Onasch et al.*, 2015], 10 % accuracy in scattering calibration (based on the SD of multiple calibrations), $\pm 1\,\mathrm{Mm}^{-1}$ baselining accuracy and 5 % accuracy in dilution correction. The fraction of scattered light not collected by the CAPS PMssa integrating sphere (the truncation error) must be corrected for if the phase function of measured particles is substantially different to that of the calibration particles. This is not the case if both measured and calibration particles are small relative to the 780 nm wavelength of the CAPS *Onasch et al.* [2015], which was generally true. Any potential complications introduced by the larger BC mode in HFO PM are unlikely, considering the fact that the HFO data were not outliers in the optical analyses described below. We note that the calculated absorption is not highly sensitive to truncation errors at low SSA values (~ 0.7.)
- For the SP2, the relatively low number of rBC particles measured in each sampling period yielded substantial statistical imprecision, which is the major source of reported uncertainty. Calibration-related uncertainties were not propagated into the reported uncertainties; the precision of our calibration data was much less than the just-mentioned statistical imprecision. An unknown source of uncertainty is calibration bias related to differences between calibrant and sample. To the extent that marine-engine rBC is similar to road-vehicle rBC, the latter bias is estimated as $< 14\%$ [*Laborde et al.*, 2012b].
- For the AMS, a measurement precision of $0.3\,\mu\mathrm{g\,m}^{-3}$ was estimated from measurements of filtered air and combined with the statistical imprecision of the mean. Measured concentrations may have been biased low by $\sim$ 10 to 35 %, for smaller particles, due to the small measured particle sizes (e.g. $\sim$ 60 nm mode diameter of volume distributions). This size-dependent bias was discussed by *Liu et al.* [2007]. Other known biases [*Jimenez et al.*, 2016] include variability in the electron ion-

ization efficiency of different organic molecules and the partial loss of particles to bounce off of the heated vaporizer. The former effect was treated as negligible and the latter estimated as negligible since these particles contained a substantial amount of lubrication oil [*Eichler et al.*, 2017], which as a liquid is unlikely to bounce [*Jimenez et al.*, 2016].

- An estimated inaccuracy of $\sigma_{\mathrm{AAE(BC)}} = 0.1$ was propagated into the calculated uncertainties of $b_{\mathrm{abn,brC},\lambda}$.
- In calculating k_{OM}, estimated imprecisions of 5 nm in GMD, 0.1 in GSD, and 4 % in density (from the SD of multiple measurements) were considered as Gaussian and propagated by Monte Carlo calculation.

3 Results and discussion

3.1 Engine emissions

The emission factors relative to engine power (in units of mg / kWh) for OM, sulfates, rBC and nitrates from this engine were similar to those reported by *Mueller et al.* [2015] for this engine. For all three fuels, OM emissions dominated the total PM mass with little sensitivity to engine load. For HFO, OM contributed 58 % of the $PM_{2.5}$ mass at 50 % load (because sulfate contributed 25 %) and > 82 % of the $PM_{2.5}$ mass below 50 % load. Notably, when normalized to CO_2 rather than engine power, the variability in emission factors for rBC was substantially reduced. Section S1 provides more detail on these emission factors.

3.1.1 Total & BC size distributions

Particle number and volume size distributions, as measured by SMPS as a function of mobility diameter d_{mob}, are shown in Fig. 3. Also shown in these figures are the number and volume distributions of rBC cores, as measured by SP2 as a function of d_{rBC}. These size distributions are representative averages of selected measurement periods, where both SMPS and SP2 data were available.

The size distributions of the diesel fuel (DF) and marine gas oil (MGO) PM, shown in Fig. 3, were comparable to that of typical diesel engines [*Burtscher*, 2005], in that two separate modes are identifiable, a volatile ultrafine mode (at about 60 nm d_{mob} in the total-volume distribution) and a soot mode (lognormal at about 120 nm d_{rBC} in the rBC-volume distribution) were observed. AMS measurements of the fresh and thermodenuded aerosol indicated that the ultrafine mode for these distillate fuels consisted mainly of organics and, for MGO, sulfates. The rBC volume distribution indicated that a fraction of the MGO and DF particles was above or below the quantification range of the SP2, corresponding to an unmeasured mass fraction of < 3 % (above) and < 23,% (below), respectively. The rBC mass concentrations reported from these SP2 data have been corrected for this missing fraction, as discussed further at the end of this subsection.

In considering Fig. 3 relative to previous studies [*Oeder et al.*, 2015; *Mueller et al.*, 2015; *Streibel et al.*, 2017], it is important to realize that the SP2-measured d_{rBC} is a volume equivalent diameter, which is by definition smaller than d_{mob} for soot particles of both open and compact morphologies [*Kulkarni et al.*, 2011]. For the two size distributions in Fig. 3 to overlap, a size-independent shape factor of $\sim$ 2.2 is required. This value is within the range of values (1.5–3) recommended by *Sorensen* [2011] for uncoated, fractal-like BC aggregates, and corresponds to $\sim$ 50 primary particles in a typical BC aggregate, if the monomer diameter is 30 nm [this monomer diameter is from *Oeder et al.*, 2015]. Thus, our measured size distributions are consistent with the evidence presented in Section 3.1.2 to demonstrate that rBC was externally mixed.

The size distribution of the residual fuel, HFO, also showed an ultrafine mode consisting of sulfates and organics with a mode diameter of about 90 nm. This mode dominated the overall particle number and had a mean ($\pm$ SD) effective density of 1460 $\pm$ 50 kg m^{-3}. The effective density was considerably lower for MGO, at 890 $\pm$ 30 kg m^{-3} (data shown in Fig. 3). The effective densities for DF PM was not measured. Since the particles consisted of organics and sulfate (see also Section 3.1.2) they were liquid [*Seinfeld and Pandis*, 2012], and these effective densities correspond directly to the material density of this PM mode. We could not obtain effective density measurements of rBC-containing particles due to their relatively low number concentrations.

The rBC-core distribution showed a much broader volume distribution than is expected for vehicular [*Burtscher*, 2005; *Laborde et al.*, 2012c], biomass burning [*Schwarz et al.*, 2008; *Laborde et al.*, 2012c; *Wang et al.*, 2016], or aircraft [*Lobo et al.*, 2015] emissions. Two studies of Chinese air pollution have also reported large rBC modes of 690 nm [*Huang et al.*, 2011] and 610 nm [*Wu et al.*, 2017], which may be linked to HFO-combustion pollution. In HFO exhaust from a marine diesel engine, *Kasper et al.* [2007] also observed a large, non-volatile (at 400°C) mode, but did not measure its chemical composition. Our measurements show that at least part of this mode consists of rBC. It likely comprised the char particles defined in the introduction. Future studies should further explore the properties of this large rBC mode.

The SP2 did not measure the tail of the hypothesized char mode (larger rBC mode). In the laboratory, *Linak et al.* [2000] found that char particles produced from HFO had a typical diameter of 1 μm, which may correspond to the significant mass fraction of PM that has been identified in the coarse mode of marine engines [*Fridell et al.*, 2008]. Therefore, we initially hypothesized that the SP2 may not have measured all BC mass in the aerosol. However, we did not find supporting evidence for this hypothesis, as discussed in the following paragraphs.

A simple test of this hypothesis may be performed using the SP2 data directly. At the upper limit of single-particle mass, single particles are measured as saturated signals in the SP2. For the HFO size distribution presented in Fig. 3 only 5 of 350,000 particles caused saturated signals. Therefore, the majority of the PM passing through our sampling system (which included a $PM_{2.5}$ cyclone) and reaching the SP2 was measured. This

conclusion is corroborated by the excellent correlation between CAPS PMssa and SP2 (Fig. S1 and S2), for which data were available only for selected experiments.

Another test of this hypothesis was performed using Mie calculations of the AAE(880,950) for BC and for cenospheres. We chose this wavelength pair so that absorption by canonical brC would be negligible [*Laskin et al.*, 2015]. Cenospheres are core-shell BC particles with air cores and have been observed in HFO PM [e.g., *Chen et al.*, 2005]. They may be modelled accurately with core-shell Mie theory [*Huang et al.*, 2012], which we have done in Fig. S3. The cenospheres were modelled with a ratio of inner to outer diameters of 0.8 (the abscissa of Fig. S3 is the outer diameter).

The Mie calculations (Fig. S3) show that in the Rayleigh regime (diameter $d < 30\,\mathrm{nm}$) the predicted $\mathrm{AAE_{BC}} \approx 1$ does not depend on the model, as expected. Outside of the Rayleigh regime ($d > 400\,\mathrm{nm}$), the model becomes important; in our calculations the $\mathrm{AAE_{BC}} \approx 0$. The calculated $\mathrm{AAE_{BC}} \approx 0$ is much smaller than our observed AAE(880,950) ≥ 1 (also shown in the figure), suggesting that the majority of BC absorption and therefore BC mass did not reside in unmeasured char particles.

Overall, the HFO rBC size distribution could be described by a bimodal lognormal fit with geometric mean d_{rBC} and standard deviations (GMD and GSD) of 150 and 640 nm, and 1.0 and 0.56, for the two modes. These lognormal fits imply that 44 % of the total mass was likely above (versus 2 % below) the particle size range detectable by the SP2 and were used to correct the total reported rBC mass. The corresponding SP2-mass correction factor was 1.46 ± 0.15. This uncertainty represents inter-experiment variability and was propagated into the overall uncertainty. For unimodal lognormal fits to the diesel and MGO data, the correction factors were 1.247 ± 0.05 and 1.228 ± 0.05, respectively. These latter correction factors account for particles which were too small to be measured by the SP2.

3.1.2 External mixing of rBC and OM/sulfate

Fig. 4A and 4B investigate the coating thickness on BC particles by analyzing the time-resolved SP2 scattering signals in two different ways. Fig. 4A shows that the number fraction of particles with evidence of 'thick coatings' (where the peak scattering signal occurs before particle incandescence, indicating the loss of a large volume of coating material due to heating) was negligible except for smaller DF particles. (Since no brC absorption was observed for DF, this exception does not influence any of the conclusions made in this study.) The remainder, 'moderate or no coating", describes particles where peak scattering occurred simultaneously with incandescence. This delay-time analysis provides a relatively coarse picture of the mixing state of BC; more quantitative information is provided by the coating-thickness analysis.

Fig. 4B shows the results of the SP2 coating-thickness analysis. For this analysis, only BC particles with spherical-equivalent diameter $240 \pm 20\,\mathrm{nm}$ were included, due to the need to optimize both counting statistics and signal-to-noise in the SP2 detectors.

Consistent with the delay-time analysis, the coating-thickness results show that the mean coating thickness for HFO particles was negligible, whereas small amounts of coatings may have been present for MGO and DF. Negative coating thicknesses reflect particle-to-particle errors (biases) in the scattering measurements, which average to zero. Note that an order of magnitude more data were available for the HFO analysis than for the other fuels analysis. In all cases, the analysis indicates that the coatings were not thick enough to influence the optical properties of the BC [*Liu et al.*, 2017].

Further analysis of independent size-resolved composition measurements for HFO [*Corbin et al.*, 2017] support this picture. Ash (metal oxides and/or sulfates) is also expected in the HFO PM, as discussed in *Corbin et al.* [2017]. However, with the measurements presented here, we can only infer that ash particles did not make up the majority of the total particle mass for either rBC or OM/sulfate particles.

The effective density measurements for the mobility size range 60 – 120 nm shown in Fig. 3 also support our conclusion that the smaller mode in that figure consisted of externally-mixed OM (and sulfate, in the case of HFO) . The effective densities (calculated as $6m_p/[\pi d^3_{\text{mobility}}]$, where m_p is the APM-measured single-particle mass and d_{mobility} is the DMA-selected diameter, as further described in the supplement) are shown by the inset circles in Fig. 3. For MGO and DF, these densities should correspond to the material density of the OM in those fuels. Indeed, the measurements are in close agreement with the densities predicted from a published empirical relationship between the elemental composition and the density of OM [*Kuwata et al.*, 2012]. That parameterization showed a low bias of just 5 % (standard deviation 2 %) relative to the DMA-APM-CPC measurements.

3.1.3 Relationship of BC light absorption with $SSA_{780\,nm}$ and engine load

BC light absorption was characterized according to the aerosol light absorption coefficient measured at 780 nm, $b_{\text{abn,780nm}}$, which was measured by the CAPS PMssa using the extinction-minus-scattering technique. The measured extinction and scattering coefficients also provided the aerosol single-scattering albedo ($SSA_{780\,nm}$; Fig. 5A). All three fuels showed a range of $SSA_{780\,nm}$ (from 0.5 to 0.9). The lower SSAs correspond to conditions where the extinction-minus-scattering method results in a more accurate calculation of $b_{\text{abn,780nm}}$.

The ratio of CAPS $b_{\text{abn,780nm}}$ to SP2 C_{rBC} gives the $MAC_{BC,780nm}$ (Eq. 3), as shown in Fig. 5B. The $MAC_{BC,780nm}$ did not vary substantially between engine loads or fuel types. The $SSA_{780\,nm}$ did vary substantially, but without a clear dependence on engine load, fuel type, or indeed any other parameter we evaluated, including the GMD (geometric mean diameter of the FMPS) and the ratio BC:non-refractory-PM. These quantities were explored because it was expected that the $MAC_{BC,780nm}$ and $SSA_{780\,nm}$ would vary as a function of aerosol composition (for example, the mass fraction of BC), size (since scattering depends strongly on particle size), or mixing state (since internal mixing of BC with other material may result in absorption enhancements). Note that although the

accuracy of the CAPS-estimated $b_{abn,780nm}$ is expected to decrease with increasing SSA, our data indicate that this accuracy was not a limiting factor: there was no statistically-significant dependence of the $MAC_{BC,780nm}$ on the SSA.

The lack of any such observed relationship indicates that the corresponding phenomena were not the main cause of variations in the $SSA_{780\,nm}$. Moreover, the fact that variations in $SSA_{780\,nm}$ did not correspond to variations in $MAC_{BC,780\,nm}$ is consistent with the aerosol containing a variable fraction of externally-mixed BC. We therefore hypothesize that variable amounts of externally-mixed ash particles were the main cause of the variability in the $SSA_{780\,nm}$. Such ash particles were identified by electron microscopy in these samples [*Corbin et al.*, 2017], but more data would be needed to quantitatively evaluate this hypothesis.

The shading in Fig. 5B shows the result of an uncertainty-weighted orthogonal-distance regression fit to a plot of $b_{abn,780nm}$ vs C_{rBC} (the shading shows the fit ± 95% confidence interval; Fig. S1). As there was no apparent difference in $MAC_{BC,780\,nm}$ between different fuels, all data were fit simultaneously to yield $MAC_{BC,780\,nm} = 7.8 \pm 1.8\,m^2\,g^{-1}$. Assuming an AAE_{BC} of 1, this corresponds to a $MAC_{rBC,550\,nm}$ of 11.1 ± 2.6, a factor 1.48 larger than the widely-accepted $MAC_{BC,550\,nm} = 7.5\,m^2\,g^{-1}$ recommended by *Bond and Bergstrom* [2006] for uncoated BC.

An increase in MAC due to so-called lensing effects may occur if rBC is internally-mixed with substantial amounts of non-absorbing material [*Liu et al.*, 2017]. However, our SP2 measurements indicate that much more internal mixing than observed would be necessary to explain a 48 % lensing enhancement (Fig. 4). The calculated absorption enhancement for a 240 nm rBC core is shown on the upper axis of Fig. 4, using a Mie approximation. For HFO, a negligible enhancement is predicted. For MGO and DF, a maximum absorption enhancement of 10–20 % is predicted. Further calculations verified that these enhancements change negligibly when the soot aggregates are represented as non-interacting monomer spheres, instead of volume-equivalent spheres [*Liu et al.*, 2015]. Considering the uncertainties associated with the coating-thickness and MAC data, we consider that the discrepancy between the calculated and apparent absorption enhancements is probably negligible for MGO and DF. For HFO, where our confidence is enhanced by a larger number of analyzed particles, we find that lensing does not explain the why the $MAC_{rBC,780\,nm}$ was higher than expected. Further work is needed to clarify why this HFO $MAC_{rBC,780\,nm}$ was higher than previously-reported values.

Some difference in $MAC_{rBC,780\,nm}$ for HFO compared to the distillate fuels may have been anticipated due to the presence of a large rBC mode in HFO PM (Section 3.1.1). This was not observed. One may therefore hypothesize that all rBC particles consisted of soot aggregates, since the $MAC_{rBC,780\,nm}$ of a soot aggregate depends primarily on the size of its monomers [*Sorensen*, 2001] and not on its overall size. However, as measurements on char particles are lacking in the literature, it is not clear that the $MAC_{rBC,780\,nm}$ (and other optical properties) of small char particles would be sufficiently different from soot to be seen in Figs. 5B and S1. Regardless of the physical interpretation, our data

indicate that the anomalous size distribution of HFO PM did not lead to an anomalous $MAC_{rBC,780\,nm}$. We note, however, that SP2 measurements were not available for the lowest engine load test points, for which brC absorption appeared to be anomalously high.

3.2 Brown carbon

In this section, we discuss the wavelength-dependence and intensive properties of brown carbon (brC). The focus is on HFO PM, since brC was negligible in the other fuels.

We reiterate here that these calculations are numerically independent of the SP2 data discussed in Section 3.1.1, as shown in the schematic diagram Fig. 2. Uncertainties related to the larger mode of rBC particles measured in HFO PM by SP2 are therefore irrelevant to the following results. In particular, we used only the $b_{abn,780nm}$ measured by CAPS PMssa and the AAE measured by the AE33 to calculate k_{OM}. The assumptions are that AAE_{BC}= 1 and that only BC absorbs at $\lambda > 700$ nm.

3.2.1 Wavelength dependence of light absorption

Fig. 6 shows AE33 absorption spectra for all engine test points. The data are normalized to 880 nm to allow different concentrations to be compared. The distillate fuels (DF and MGO) show similar trends and are consistent with an AAE of 1 ± 0.1 down to 470 nm. At 370 nm, there is some evidence of a minor contribution ($<$ 20 % of b_{abn} at 370 nm) of brC to light absorption for the distillate fuels.

For HFO, the data are generally consistent with an AAE(370–950) of 1.7 ± 0.2. The shaded region in Fig. 6 encompasses this range, showing that this AAE includes the majority of the data points while slightly underpredicting absorption at $\lambda < 500$ nm. We hypothesized that the scatter in Fig 6 may be related to a varying mass fraction of BC (relative to OM and sulfate) but found this this was not the case (Fig. S4).

Fig. 6 also includes MWAA measurements of light absorption of the filter samples. These spectral measurements provide additional confidence in the AE33 data, since the MWAA directly measures and corrects for light scattering from the filter sample. The MWAA data represent only three HFO filter samples due to limited sample availability, but generally corroborate the AE33-measured AAEs.

3.2.2 $MAC_{OM,370}$

Fig. 7C shows brC absorption at 370 nm, per mass of OM ($MAC_{OM,370}$) for all fuels as a function of engine load. For cases in which the median AE33 C value was used, rather than a specifically-calibrated C-value, the data are shown with open rather than filled symbols. The upper panel, Fig. 7A, illustrates the AE33-measured AAEs from which these MACs have been derived.

Fig. 7C shows that the $MAC_{OM,370}$ increased by an order of magnitude at the lowest engine load for HFO. This increase did not correspond to a change in the overall OM emission factor EF_{OM}, as seen by comparison to Fig. 7B, nor to a change in the sampled OM concentrations (not shown). Therefore, this change must be due to a difference in the chemical composition of the OM. For this reason, we hypothesized that the less-volatile thermal–optical OC fractions would correlate with $MAC_{OM,370}$, but found that the correlation was poor (Section S5). The relative emission factors of polycyclic aromatic hydrocarbons (PAHs), including oxygenated- and nitrogenated PAHs, have been reported to increase at low engine loads by *Sippula et al.* [2014]. Such species have been connected to the chemical composition of the fuel [*Rüger et al.*, 2015; *Streibel et al.*, 2017]. The optical properties are thus not adequately described by the lubricating-oil model proposed by *Eichler et al.* [2017], who only discussed engine emissions at 50 % load.

3.2.3 Imaginary refractive index of OM, $k_{OM,\lambda}$

Based on the measurements described in the previous sections, a Mie model was constructed and fit to the data to obtain the imaginary refractive index of OM for this study, as detailed in Section 2.5.

Figs. 8 and 9 show the results of the Mie model fits. Fig. 8 shows $k_{OM,370}$ as a function of $MAC_{OM,370\,nm}$. The two quantities are correlated because the main variations in model inputs were in OM mass concentration and light absorption, rather than particle size or density. Two extreme outliers have a $k_{OM,370}$ close to unity, which is unusually high. We carefully inspected all input data for these measurements but found no errors. The $k_{OM,370}$ for DF and MGO were not significantly different from zero.

Fig. 9 depicts the wavelength dependence of k_{OM} by normalizing $k_{OM,\lambda}$ to $k_{OM,370}$ for all data. The grey shading and lines show the behaviour that would be expected for a k_{OM} AAE of 2, 3, and 4 (upper line, central line, lower line). The plot was filtered to only included points where $k_{OM,\lambda} > 0.005$ before normalization. This threshold is based on the Monte-Carlo-estimated uncertainties shown in Fig. 8 and resulted in the exclusion of all MGO and DF data.

Two types of outliers are noticeable in Fig. 9. The first, "outlier I", shows an anomalously slow decrease in k_{OM} with λ. The reason for this exception was not identified. The second, "outlier II", correspond to the two high outliers in Fig. 8. The k_{OM}-versus-λ trend for both of these type-II outliers appears reasonable and is similar; compared to the other measurements the slope is more negative than expected. In other words, in addition to having higher absolute $k_{OM,370}$ these measurements also had a higher ratio $k_{OM,370} : k_{OM,660}$, which is consistent with a true chemical difference in the type-II samples.

4 Discussion

4.1 Expected differences between engines and HFO samples

In general, the intensive optical properties of marine-engine PM may vary between studies. In our present study, we have observed similar trends to those observed in the study described by *Mueller et al.* [2015], as discussed in detail in Section S5. Further measurements are required to investigate the degree to which engine-to-engine variability may influence these properties.

In addition, differences in fuel composition may influence marine-engine PM optical properties. Since the molecular composition of HFO PM has been shown to be comparable with the molecular composition of HFO [*Streibel et al.*, 2017], in a manner depending on engine load [*Sippula et al.*, 2014], we hypothesize that the molecular composition of brC is also related to the molecular composition of the fuel. In support of this hypothesis, we note that *Sippula et al.* [2014] observed larger mass fractions of PAHs in HFO OM at lower engine loads, similar to our observation of increased $\mathrm{MAC_{OM}}$ at lower engine loads. Those authors suggested that the PAHs in HFO PM represent unburned fuel. This picture is consistent with the non-absorbing nature of the distillate-fuel PM samples, since neither MGO nor DF contain substantial levels of PAHs.

If PAHs in HFO are a major source of brC in HFO PM, then different engines may produce brC in a similar manner to one another. Thus, the extrapolation of the $\mathrm{MAC_{OM}}$ and k_{OM} reported herein to other engines may be justified, especially when using the relationship of OC3 / OC with $\mathrm{MAC_{OM,370}}$ (Fig. S5) to estimate light-absorption by brC in HFO PM. However, since variability in the composition of HFO fuel [*Stout and Wang*, 2016] may lead to variability in the light-absorbing properties of the emissions, additional studies are warranted to constrain fuel-related variability in k_{OM} and $\mathrm{MAC_{OM}}$.

4.2 Summary and implications of brC / OM light absorption

In the following, we summarize the results on brC absorption and provide an illustration of the potential radiative impacts of HFO brC.

The standard operating load for this engine is 50 %, although engines frequently operate at lower loads to save fuel or in the presence of ice [*Lack and Corbett*, 2012]. At 50 % load, the mean $k_{\mathrm{OM,370nm}}$ and corresponding SD were 0.057 ± 0.027 ($n = 5$). At 25 % load, the corresponding values were 0.034 ± 0.018 ($n = 6$). Considering the large variabilities, we recommend the combined mean, 0.045 ± 0.025, for modelling studies. According to Fig. 9, $k_{\mathrm{OM},\lambda}$ may then be estimated as

$$k_{\mathrm{OM},\lambda} = (0.045 \pm 0.025)(\lambda/370\mathrm{nm})^{-3}, \qquad 370\,\mathrm{nm} < \lambda < 660\,\mathrm{nm} \tag{6}$$

At the commonly-used λ of 550 nm, Equation 6 gives $k_{\mathrm{OM,550nm}} = 0.014 \pm 55\,\%$. Compared to the $k_{\mathrm{OM,550nm}}$ values summarized by the review of *Lu et al.* [2015], this is a

high value. For example, those authors recommended $k_{\mathrm{OM,550nm}} = 0.015 \pm 45\,\%$ for lignite OM and $k_{\mathrm{OM,550nm}} \approx 0.03$ for biomass-combustion OM with 10 % BC (a comparable fraction to our data). For HFO, *Lu et al.* [2015] recommended $k_{\mathrm{OM,550nm}} = 0.006 \pm 40\,\%$, based on the extrapolation of studies of DF emissions to HFO. This is a factor of 2.3 smaller than our measured value. Considering that we measured negligible brC for DF PM, this extrapolation is not valid and future studies should use Equation 6 to estimate k_{OM} for HFO.

The very high OM fraction (approximately 90 %) in HFO emissions makes brC light absorption especially important for this aerosol in spite of its k_{OM} falling within the range of previously-reported values (at 25–50 % engine load). This is demonstrated in Fig. 10, where the Simple Forcing Efficiency [*Chen and Bond*, 2010; *Bond and Bergstrom*, 2006] has been employed. The figure illustrates the Direct Radiative Forcing (DRF) of a representative ship-exhaust plume over the planet's surface. A wavelength-dependent mass scattering cross section of 2.3 $\mathrm{m^2\ g^{-1}}$ at 780 nm and scaling exponent of 4 (see supplement for details) was used with a backscatter fraction of 0.1. For the 50 % load case (inputs shown in lower panel), the figure plots the relative absorption of OM and BC (middle panel) and the estimated change in direct radiative forcing (DRF, upper panel) when including brC absorption. The change in DRF is relative to the base case of non-absorbing OM (equal OM mass, with k_{OM} set to zero). Relative humidity effects have been neglected for simplicity. The DRF is highly sensitive to the albedo of the surface below the aerosol; as such, two cases are shown: one for the case of fresh snow or cloud, one for the case of the dark ocean.

Note that OM absorption from HFO at $\lambda = 660$ nm is $\sim$ 20 % of the total. At this wavelength, brC absorption may have been expected to have dropped to zero [*Laskin et al.*, 2015]: HFO brC clearly absorbs farther into the red than expected. At $\lambda = 370$ nm, the contribution of brC to the DRF increases to 18% for the over-snow case. Note that we have chosen a conservative example of 50 % load, and that $\mathrm{MAC_{OM}}$ was much larger at lower loads (Fig. 7). The ability of brC absorption to influence the DRF of HFO-exhaust PM, particularly in high-albedo environments like the Arctic, should motivate modelling studies to assess the overall climate effects of this organic absorption.

5 Conclusions

We used in-situ measurements of single-particle black carbon mass (via laser-induced incandescence), in-situ aerosol light extinction and scattering coefficients, and filter-based measurements of Ångström absorption exponents, to reach several conclusions on the properties of BC and brC in emissions from an auxiliary-scale research ship engine. One residual fuel (heavy fuel oil; HFO) and two distillate fuels (marine gas oil, MGO, and diesel fuel, DF) were used.

Overall, light absorption by OM in DF and MGO exhaust was found to be negligible, whereas absorption by OM in HFO PM was very significant. This result is not sur-

prising considering the near-black colour of the HFO fuel (diesel is almost transparent) and the molecular similarity between HFO-exhaust OM and the fuel [*Sippula et al.*, 2014; *Streibel et al.*, 2017]. In more detail, our conclusions are as follows.

- Generally, BC was externally mixed from non-refractory material (sulfates and organics) in the primary emissions. The BC size distribution for DF and MGO was a typical lognormal, whereas for HFO an apparent bimodal lognormal with very large rBC particles was observed.
- The ratio of 780 nm light absorption coefficient with rBC mass gave a $MAC_{rBC,780\,nm}$ of $7.8 \pm 1.8\,m^2\,g^{-1}$ from SP2 and in-situ absorption measurements for all three fuels.
- The overall wavelength dependence of absorption ($370 < \lambda < 950$ nm) for this PM can be generally described by an AAE of 1.0 ± 0.1 for MGO and DF and by an AAE of 1.7 ± 0.2 for HFO.
- Considering the PM as a mixture of brC and BC with AAE_{BC}= 1 (BC+brC model), only HFO was found to contain significant amounts of brC, with $MAC_{OM,370\,nm} = 0.4 \pm 0.2\,m^2\,g^{-1}$ at typical operating conditions of 50 % load. At low engine loads (11 %), MACs up to $10\,m^2\,g^{-1}$ were observed while OM emission factors remained unchanged, indicating a fundamental change in the nature of the absorbing material.
- Using a measurement-constrained Mie model, we retrieved wavelength-dependent imaginary refractive indices $k_{OM,\lambda}$ for HFO of 0.032 – 0.066 (interquartile range). A parameterization was provided for $k_{OM,\lambda}$ at typical engine operating conditions (Eq. 6). The reported k_{OM} is large compared to previous values reported for open biomass burning [*Lu et al.*, 2015]. Due to the high OM fraction in this exhaust (~ 90 %), OM absorption (brC) may contribute up to 50 % of total absorption for HFO at 370 nm, and 20 % at 660 nm.
- A simplified calculation showed that accounting for brC in the radiative forcing of HFO PM may enhance the direct radiative forcing by 18 % at 370 nm and 50 % load, and much more at lower engine loads. Climate models should therefore include this absorption when estimating the radiative effects of ship exhaust.

Although the emissions and light-absorbing properties of OM may vary between engines, between engine settings, and between HFO samples, our reported k_{OM} and MAC_{OM} values provide a significant improvement over previously-available data.

Author contributions

JCC performed the initial data analysis and interpretation. HC, MG, IEH, GM, and LD contributed significantly to data interpretation. MZ, JCC and MG operated and calibrated the SP2. SP and JCC operated and calibrated the CAPS. GJ operated the AE33 and provided its data, LD analyzed the AE33 raw data. AAM, SP, and JCC operated and calibrated the AMS. JCC performed the APM measurements. JO and BS planned and over-

saw the experiments. ASHP and RZ initiated the study. JCC wrote the manuscript and all authors contributed to the writing.

Acknowledgments

We thank Anna Possner for input leading to the Mie model and Jonathan Taylor for the Mie program. We thank also Branka Miljevic, Nivedita Kumar, and the University of Rostock staff for their work and assistance during the measurements. This project, WOOSHI, was funded by the Swiss National Science Foundation (SNSF, project number 140590), the German research foundation (DFG, grant Zi 764/5-1), and the Helmholtz Virtual Institute "HICE – Aerosol and Health" (www.hice-vi.eu) via the Helmholtz Association (HGF-INF). JCC, MZ, and MG received financial support from the ERC under grant ERC-CoG-615922-BLACARAT. GM and LD are employed by Aerosol d.o.o., where the Aethalometer AE33 was developed and is being produced. Emission factor and brC properties data are included in the online supplementary material.

803 **Table 1.** Common abbreviations and symbols used in the text. Rarely-used abbreviations have been omitted
804 for brevity.

Abbreviation	Definition
AAE	Absorption Ångström exponent
AAE(λ_1, λ_2)	AAE calculated from two specified λ
AE33	Model AE33 Aethalometer
BC	Black carbon
rBC	refractory BC, measured by SP2
brC	Brown carbon, operationally defined by light absorption in excess of that predicted for BC.
CAPS PMssa	Cavity Attenuation Phase Shift PM SSA monitor.
AMS	Aerosol Mass Spectrometer
APM	Aerosol Particle Mass analyzer
DF	Diesel fuel (a distillate fuel)
MAC	Mass absorption cross-section of PM
MGO	Marine Gas Oil (a distillate fuel)
MWAA	Multi-Wavelength Absorption Analysis
HFO	Heavy Fuel Oil (residual fuel)
OM	The non-refractory organic component of PM, operationally defined by vaporization at 600 °C.
PM	Particulate Matter
SSA	Single-scattering albedo
SP2	Single Particle Soot Photometer
b_{abn}	Aerosol absorption coefficient
C_x	Mass concentration of x
n	Real part of the refractive index
k	Imaginary part of the refractive index
λ	Wavelength
d_{rBC}	Volume-equivalent diameter of rBC core
d_{mob}	Mobility diameter

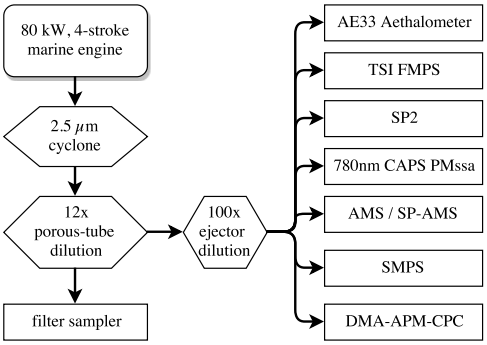

805 **Figure 1.** Experimental setup. Filter samples were measured after a factor ~ 12 dilution; other measure-
806 ments after a further factor 100 dilution.

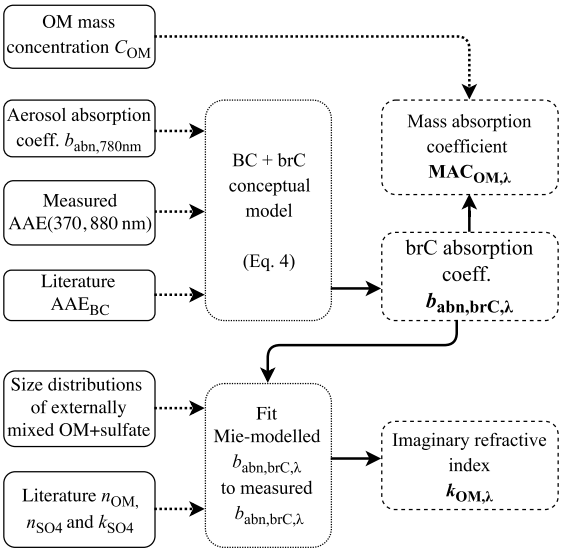

807 **Figure 2.** Schematic of the BC+brC analysis and Mie model fit performed herein. Symbols and abbrevia-
808 tions are defined in Table 1.

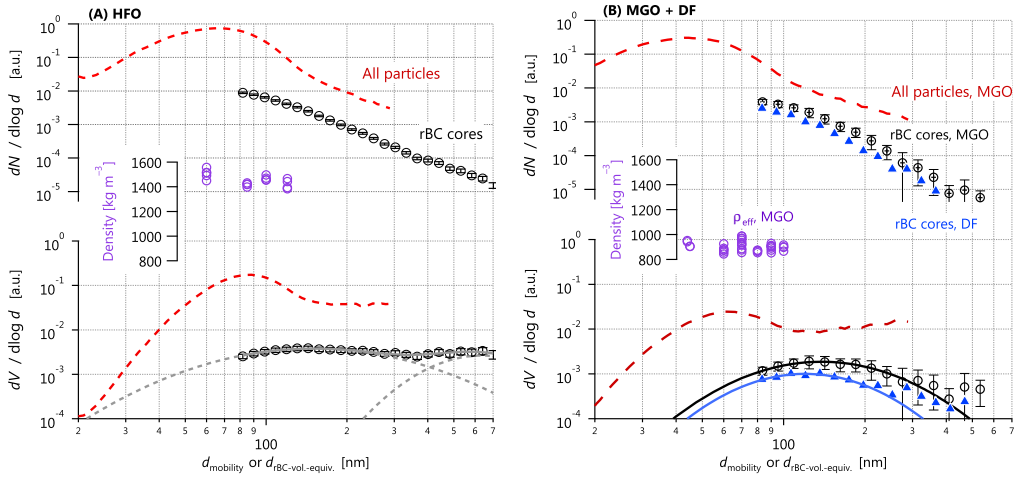

Figure 3. Size distributions of PM from the marine engine operated on (A) HFO and (B) MGO and diesel. Inset are the DMA-APM effective density data. The upper tails of the total (red; SMPS) distributions do not overlap the rBC distributions (black, blue) because of significant uncertainties in volume calculation for large, irregular particles, and because the latter is plotted against volume-equivalent rBC diameters, which are smaller than mobility diameters for coated or aspherical particles. SMPS measurements for diesel are not available.

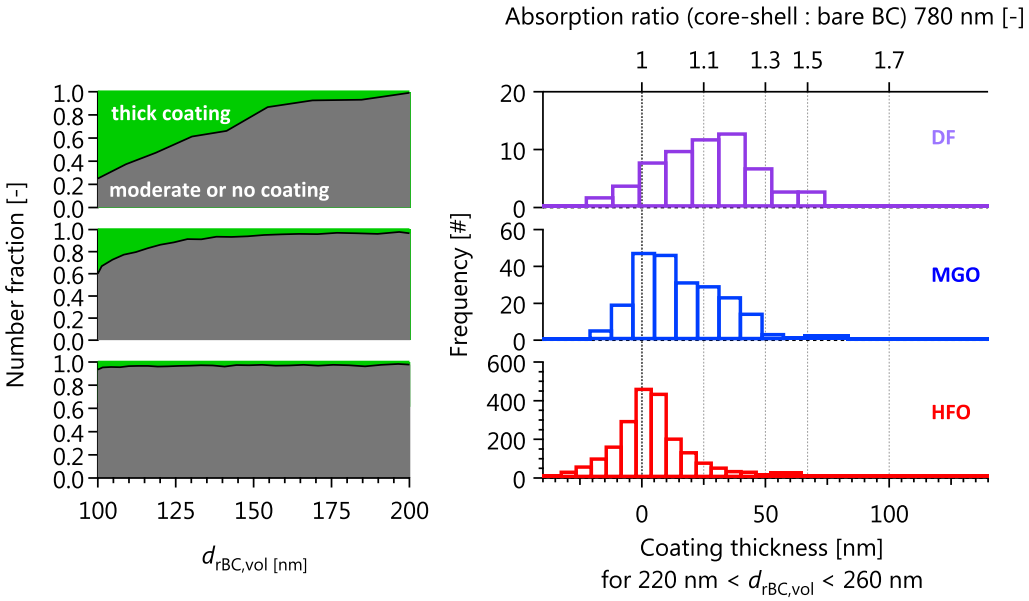

Figure 4. (A) Number fractions of particles with thick coatings versus moderate or no coatings, as determined by SP2 delay-time analysis, for BC-containing particles with d_{rBC} 100 to 200 nm. (B) SP2 coating thicknesses of BC-containing particles with d_{rBC} = 240 ± 20 nm. Negative coating thicknesses are due to noise, as discussed in the text. Note that the histogram for HFO represents an order of magnitude more data than the other fuels, due to practical constraints. Note also that different size range are shown in (A) and (B) due to the fundamental difference of the two analyses (see text). The upper axis in (B) shows the predicted core-shell-Mie absorption enhancement for these coating thicknesses at the 780 nm wavelength of the CAPS PMssa.

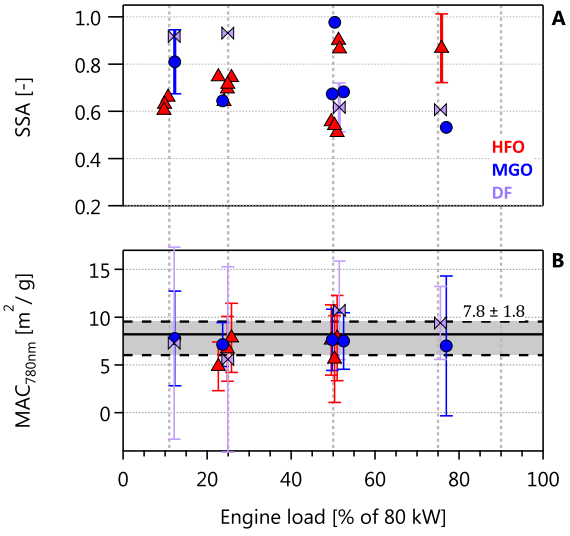

Figure 5. MAC and SSA for the three fuels as a function of engine load. No trend with engine power or fuel is apparent. Only three error bars are shown in (A) for clarity. The shaded area in (B) reflects a $MAC_{rBC,780nm}$ of 7.8 ± 1.8 $m^2\ g^{-1}$ (fit ± standard error).

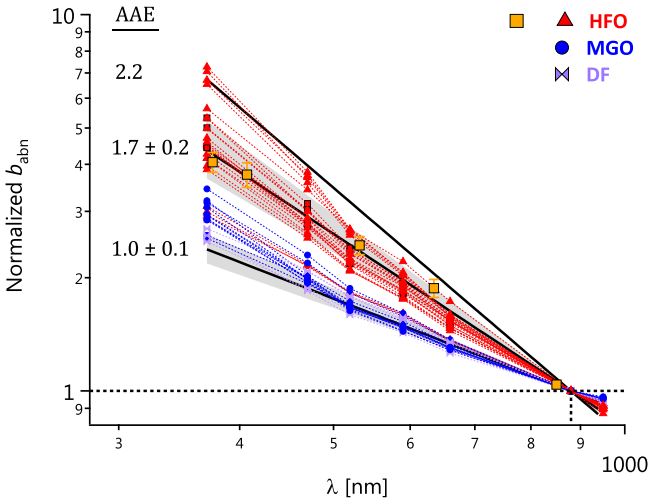

826 **Figure 6.** Measured absorption spectra for all engine test points, normalized to 880 nm. The black lines
827 and shading indicate power laws (AAEs) and uncertainties of 2.2, 1.7 ± 0.2, and 1.0 ± 0.1, as labelled. All
828 data are from the AE33 except the orange squares, which are MWAA measurements of filter samples (using a
829 normalization factor of 0.96 to adjust from 850 to 880 nm using AAE=1.7; simultaneous AE33 measurements
830 are highlighted with red squares).

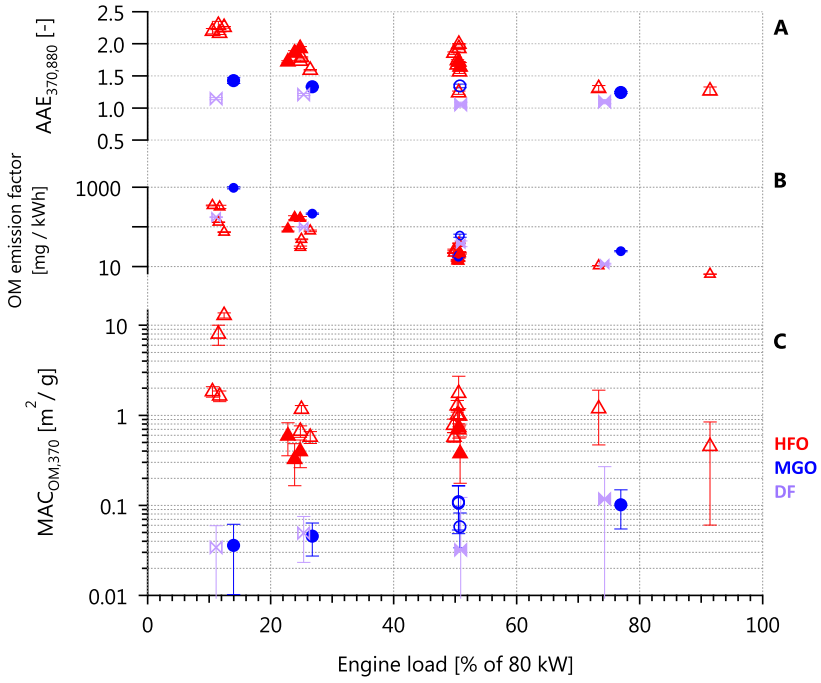

Figure 7. (A) AAEs between 370 and 880 nm, (B) OM emission factors, and (C) brC MAC (referencing total OM) plotted against engine load for the 3 fuels. In (C), open symbols indicate the use of the median rather than the CAPS-PMssa-measured AE33 C value. Fewer MAC_{OM} data points than b_{abn} data points are reported due to some missing C_{OM} measurements. Note that the increase of the MAC at 11 % engine load does not correspond to an increase of the OM emission factor. Note also the log scales.

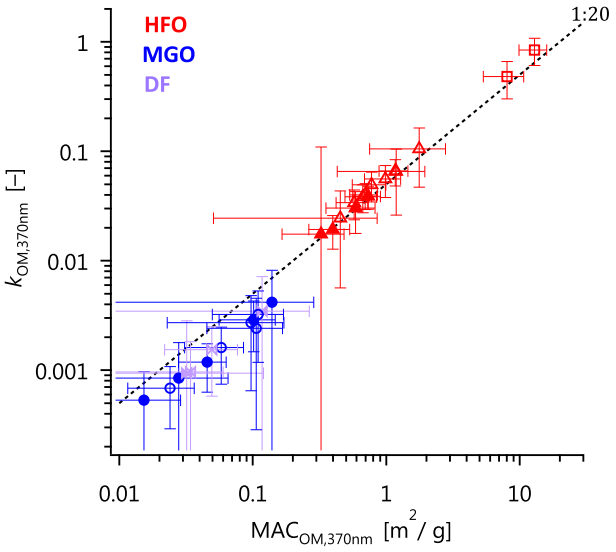

Figure 8. Retrieved OM imaginary refractive indices plotted against MAC at 370 nm. The two high-valued outliers (square symbols) represent 11 %-load conditions (see Fig. 7). The observed good correlation indicates that variability in k_{OM} was driven by variability in the OM properties (particularly engine conditions) rather than particle size or other Mie-model parameters.

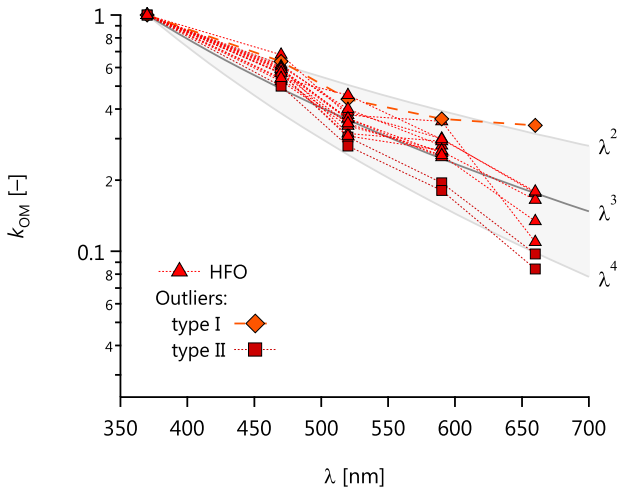

Figure 9. Retrieved imaginary refractive indices as a function of wavelength, normalized to $k_{OM,370\,nm}$. Data where $k_{OM,\lambda} < 0.005$ were omitted due to unreliable data (see error bars in Fig. 8). Outlier type I refers to the high outlier at 660 nm; outlier type II refers to the two high-k_{OM} cases shown in Fig. 8. The labels λ^x refer to power laws with exponent x. A power law with x between −2 and −4 adequately describes the data.

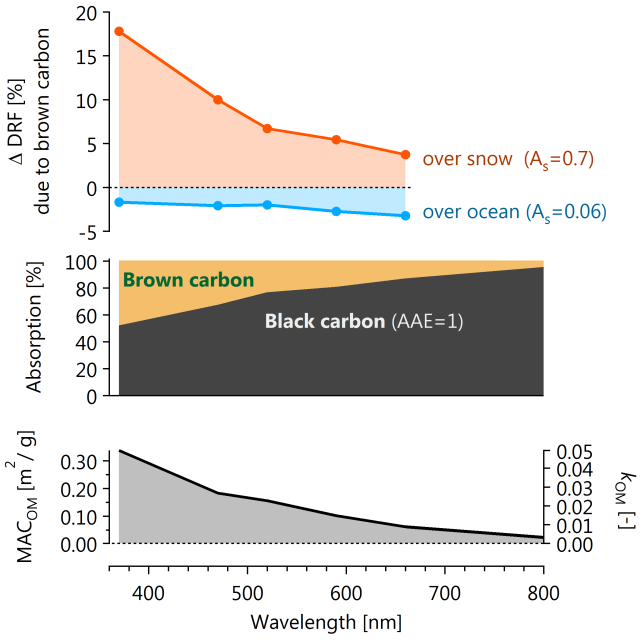

Figure 10. Depiction of the importance of brown carbon absorption for a typical case at 50 % load. Here, brC is defined by the BC+brC approach as excess absorption after subtracting BC absorption via $AAE_{BC,880\,nm}$= 1. (top) Percent change in direct radiative forcing (DRF) due to brown carbon, relative to a reference case of non-absorbing organics. (middle) Contribution of organics and black carbon to overall absorption. (bottom) MAC_{OM} and k_{OM} used for this analysis.

References

Abo Riziq, A., C. Erlick, E. Dinar, and Y. Rudich (2007), Optical properties of absorbing and non-absorbing aerosols retrieved by cavity ring down (crd) spectroscopy, *Atmos. Chem. Phys.*, *7*(6), 1523–1536, doi:10.5194/acp-7-1523-2007.

Bahadur, R., P. S. Praveen, Y. Xu, and V. Ramanathan (2012), Solar absorption by elemental and brown carbon determined from spectral observations, *P. Patl. Acad. Sci. USA*, *109*(43), 17,366–17,371, doi:10.1073/pnas.1205910109.

Bond, T. C., and R. W. Bergstrom (2006), Light absorption by carbonaceous particles: An investigative review, *Aerosol Sci. Technol.*, *40*(1), 27–67, doi:10.1080/02786820500421521.

Buffaloe, G., D. Lack, E. Williams, D. Coffman, K. Hayden, B. Lerner, S.-M. Li, I. Nuaaman, P. Massoli, T. Onasch, et al. (2014), Black carbon emissions from in-use ships: a california regional assessment, *Atmos. Chem. Phys.*, *14*(4), 1881–1896, doi:10.5194/acp-14-1881-2014.

Burtscher, H. (2005), Physical characterization of particulate emissions from diesel engines: a review, *J. Aerosol Sci.*, *36*(7), 896–932, doi:10.1016/j.jaerosci.2004.12.001.

Cazorla, A., R. Bahadur, K. Suski, J. F. Cahill, D. Chand, B. Schmid, V. Ramanathan, and K. Prather (2013), Relating aerosol absorption due to soot, organic carbon, and dust to emission sources determined from in-situ chemical measurements, *Atmos. Chem. Phys.*, *13*(18), 9337–9350, doi:10.5194/acp-13-9337-2013.

Chen, Y., and T. Bond (2010), Light absorption by organic carbon from wood combustion, *Atmos. Chem. Phys.*, *10*(4), 1773–1787.

Chen, Y., N. Shah, A. Braun, F. E. Huggins, and G. P. Huffman (2005), Electron microscopy investigation of carbonaceous particulate matter generated by combustion of fossil fuels, *Energy & Fuels*, *19*(4), 1644–1651, doi:10.1021/ef049736y.

Corbett, J. J., J. J. Winebrake, E. H. Green, P. Kasibhatla, V. Eyring, and A. Lauer (2007), Mortality from ship emissions: a global assessment, *Environ. Sci. Technol.*, *41*(24), 8512–8518, doi:10.1021/es071686z.

Corbin, J. C., A. A. Mensah, S. M. Pieber, J. Orasche, B. Michalke, M. Zanatta, H. Czech, D. Massabò, C. Buatier de Mongeot, C. Mennucci, I. El Haddad, N. K. Kumar, B. Stengel, Y. Huang, R. Zimmermann, A. S. H. Prévôt, and M. Gysel (2017), Trace metals in soot and $pm_{2.5}$ from heavy-fuel-oil combustion in a marine engine, *submitted to Environ Sci Technol*.

DeCarlo, P. F., J. R. Kimmel, A. Trimborn, M. J. Northway, J. T. Jayne, A. C. Aiken, M. Gonin, K. Fuhrer, T. Horvath, and K. S. Docherty (2006), Field-deployable, high-resolution, time-of-flight aerosol mass spectrometer, *Anal. Chem.*, *78*(24), 8281–8289, doi:10.1021/ac061249n.

Drinovec, L., G. Močnik, P. Zotter, A. S. H. Prévôt, C. Ruckstuhl, E. Coz, M. Rupakheti, J. Sciare, T. Müller, A. Wiedensohler, and A. D. A. Hansen (2015), The" dual-spot" aethalometer: an improved measurement of aerosol black carbon with real-time loading compensation, *Atmos. Meas. Tech.*, *8*(5), 1965–1979, doi:10.5194/amt-8-1965-2015.

Eichler, P., M. Müller, C. Rohmann, B. Stengel, J. Orasche, R. Zimmermann, and A. Wisthaler (2017), Lubricating oil as a major constituent of ship exhaust particles, *Environ. Sci. Technol. Let.*, *4*(2), 54–58, doi:10.1021/acs.estlett.6b00488.

Endresen, Ø. (2003), Emission from international sea transportation and environmental impact, *Journal of Geophysical Research*, *108*(D17), doi:10.1029/2002jd002898.

Eyring, V., I. S. Isaksen, T. Berntsen, W. J. Collins, J. J. Corbett, O. Endresen, R. G. Grainger, J. Moldanova, H. Schlager, and D. S. Stevenson (2010), Transport impacts on atmosphere and climate: Shipping, *Atmos. Environ.*, *44*(37), 4735–4771, doi:10.1016/j.atmosenv.2009.04.059.

Favez, O., S. C. Alfaro, J. Sciare, H. Cachier, and M. M. Abdelwahab (2009), Ambient measurements of light-absorption by agricultural waste burning organic aerosols, *J. Aerosol Sci.*, *40*(7), 613–620, doi:10.1016/j.jaerosci.2009.04.002.

Fialho, P., A. Hansen, and R. Honrath (2005), Absorption coefficients by aerosols in remote areas: a new approach to decouple dust and black carbon absorption coefficients using seven-wavelength aethalometer data, *J. Aerosol Sci.*, *36*(2), 267–282, doi:10.1016/j.jaerosci.2004.09.004.

Fridell, E., E. Steen, and K. Peterson (2008), Primary particles in ship emissions, *Atmos. Environ.*, *42*(6), 1160–1168, doi:10.1016/j.atmosenv.2007.10.042.

Gao, R. S., J. P. Schwarz, K. K. Kelly, D. W. Fahey, L. A. Watts, T. L. Thompson, J. R. Spackman, J. G. Slowik, E. S. Cross, J.-H. Han, P. Davidovits, T. B. Onasch, and D. R. Worsnop (2007), A novel method for estimating light-scattering properties of soot aerosols using a modified single-particle soot photometer, *Aerosol Science and Technology*, *41*(2), 125–135, doi:10.1080/02786820601118398.

Grenfell, T. C., S. J. Doherty, A. D. Clarke, and S. G. Warren (2011), Light absorption from particulate impurities in snow and ice determined by spectrophotometric analysis of filters, *Applied Optics*, *50*(14), 2037, doi:10.1364/ao.50.002037.

Huang, X.-F., R. S. Gao, J. P. Schwarz, L.-Y. He, D. W. Fahey, L. A. Watts, A. McComiskey, O. R. Cooper, T.-L. Sun, L.-W. Zeng, M. Hu, and Y.-H. Zhang (2011), Black carbon measurements in the pearl river delta region of china, *Journal of Geophysical Research*, *116*(D12), doi:10.1029/2010jd014933.

Huang, Y., R. Zhao, J. Jiang, and K.-Y. Zhu (2012), Scattering and absorptive characteristics of a cenosphere, *Int. J. Therm. Sci.*, *57*, 63–70, doi:10.1016/j.ijthermalsci.2012.01.019.

Jimenez, J. L., M. R. Canagaratna, F. Drewnick, J. D. Allan, M. R. Alfarra, A. M. Middlebrook, J. G. Slowik, Q. Zhang, H. Coe, J. T. Jayne, and W. D. R. (2016), Comment on "the effects of molecular weight and thermal decomposition on the sensitivity of a thermal desorption aerosol mass spectrometer", *Aerosol Sci. Technol.*, *50*(9), i–xv, doi:10.1080/02786826.2016.1205728.

Kasper, A., S. Aufdenblatten, A. Forss, M. Mohr, and H. Burtscher (2007), Particulate emissions from a low-speed marine diesel engine, *Aerosol Sci. Technol.*, *41*(1), 24–32, doi:10.1080/02786820601055392.

Kondo, Y., L. Sahu, N. Moteki, F. Khan, N. Takegawa, X. Liu, M. Koike, and T. Miyakawa (2011), Consistency and traceability of black carbon measurements made by laser-induced incandescence, thermal-optical transmittance, and filter-based photo-absorption techniques, *Aerosol Science and Technology*, *45*(2), 295–312, doi:10.1080/02786826.2010.533215.

Kulkarni, G., M. Pekour, A. Afchine, D. M. Murphy, and D. J. Cziczo (2011), Comparison of experimental and numerical studies of the performance characteristics of a pumped counterflow virtual impactor, *Aerosol Sci. Technol.*, *45*(3), 382–392, doi:10.1080/02786826.2010.539291.

Kuwata, M., S. R. Zorn, and S. T. Martin (2012), Using elemental ratios to predict the density of organic material composed of carbon, hydrogen, and oxygen, *Environ. Sci. Technol.*, *46*(2), 787–794, doi:10.1021/es202525q.

Laborde, M., M. Schnaiter, C. Linke, H. Saathoff, K. Naumann, O. Möhler, S. Berlenz, U. Wagner, J. Taylor, D. Liu, M. Flynn, J. Allan, H. Coe, K. Heimerl, F. Dahlkötter, B. Weinzierl, A. G. Wollny, M. Zanatta, J. Cozic, P. Laj, R. Hitzenberger, J. P. Schwarz, and M. Gysel (2012a), Single particle soot photometer intercomparison at the AIDA chamber, *Atmos. Meas. Tech.*, *5*, 3077–3097, doi:10.5194/amt-5-3077-2012.

Laborde, M., P. Mertes, P. Zieger, J. Dommen, U. Baltensperger, and M. Gysel (2012b), Sensitivity of the single particle soot photometer to different black carbon types, *Atmos. Meas. Tech.*, *5*, 1031–1043, doi:10.5194/amt-5-1031-2012.

Laborde, M., M. Crippa, T. Tritscher, Z. Jurányi, P. DeCarlo, B. Temime-Roussel, N. Marchand, S. Eckhardt, A. Stohl, and U. Baltensperger (2012c), Black carbon physical properties and mixing state in the european megacity paris, *Atmos. Chem. Phys.*, *12*, 25,121–25,180, doi:10.5194/acp-13-5831-2013.

Lack, D., and J. Langridge (2013), On the attribution of black and brown carbon light absorption using the ångström exponent, *Atmos. Chem. Phys.*, *13*(20), 10,535–10,543, doi:10.5194/acp-13-10535-2013.

Lack, D. A., and C. D. Cappa (2010), Impact of brown and clear carbon on light absorption enhancement, single scatter albedo and absorption wavelength dependence of black carbon, *Atmospheric Chemistry and Physics*, *10*(9), 4207–4220, doi:10.5194/acp-10-4207-2010.

Lack, D. A., and J. J. Corbett (2012), Black carbon from ships: a review of the effects of ship speed, fuel quality and exhaust gas scrubbing, *Atmospheric Chemistry and Physics*, *12*(9), 3985–4000, doi:10.5194/acp-12-3985-2012.

Lack, D. A., J. J. Corbett, T. Onasch, B. Lerner, P. Massoli, P. K. Quinn, T. S. Bates, D. S. Covert, D. Coffman, B. Sierau, S. Herndon, J. D. Allan, T. Baynard, E. R. Lovejoy, A. R. Ravishankara, and E. Williams (2009), Particulate emissions from commercial shipping: Chemical, physical, and optical properties, *J. Geophys. Res.-Atmos.*, *114*(D7), doi:10.1029/2008JD011300.

Laskin, A., J. Laskin, and S. A. Nizkorodov (2015), Chemistry of atmospheric brown carbon, *Chem. Rev.*, *115*(10), 4335–4382, doi:10.1021/cr5006167.

Lauer, A., V. Eyring, J. Hendricks, P. Jöckel, and U. Lohmann (2007), Global model simulations of the impact of ocean-going ships on aerosols, clouds, and the radiation budget, *Atmos. Chem. Phys.*, *7*(19), 5061–5079, doi:10.5194/acp-7-5061-2007.

Linak, W. P., C. A. Miller, and J. O. Wendt (2000), Fine particle emissions from residual fuel oil combustion: Characterization and mechanisms of formation, *Proc. Combust. Inst.*, *28*(2), 2651–2658, doi:10.1016/s0082-0784(00)80684-0.

Lindstad, H., G. S. Eskeland, H. Psaraftis, I. Sandaas, and A. H. Strømman (2015), Maritime shipping and emissions: A three-layered, damage-based approach, *Ocean Eng.*, *110*, 94–101, doi:10.1016/j.oceaneng.2015.09.029.

Liu, D., J. W. Taylor, D. E. Young, M. J. Flynn, H. Coe, and J. D. Allan (2015), The effect of complex black carbon microphysics on the determination of the optical properties of brown carbon, *Geophys. Res. Lett.*, pp. n/a–n/a, doi:10.1002/2014gl062443.

Liu, D., J. Whitehead, M. R. Alfarra, E. Reyes-Villegas, D. V. Spracklen, C. L. Reddington, S. Kong, P. I. Williams, Y.-C. Ting, S. Haslett, J. W. Taylor, M. J. Flynn, W. T. Morgan, G. McFiggans, H. Coe, and J. D. Allan (2017), Black-carbon absorption enhancement in the atmosphere determined by particle mixing state, *Nat. Geosci.*, *10*(3), 184–188, doi:10.1038/ngeo2901.

Liu, P. S. K., R. Deng, K. A. Smith, L. R. Williams, J. T. Jayne, M. R. Canagaratna, K. Moore, T. B. Onasch, D. R. Worsnop, and T. Deshler (2007), Transmission efficiency of an aerodynamic focusing lens system: Comparison of model calculations and laboratory measurements for the aerodyne aerosol mass spectrometer, *Aerosol Sci. Technol.*, *41*(8), 721–733, doi:10.1080/02786820701422278.

Lobo, P., L. Durdina, G. J. Smallwood, T. Rindlisbacher, F. Siegerist, E. A. Black, Z. Yu, A. A. Mensah, D. E. Hagen, R. C. Miake-Lye, K. A. Thomson, B. T. Brem, J. C. Corbin, M. Abegglen, B. Sierau, P. D. Whitefield, and J. Wang (2015), Measurement of aircraft engine non-volatile pm emissions: Results of the aviation-particle regulatory instrument demonstration experiment (a-pride) 4 campaign, *Aerosol Sci. Technol.*, *0*, 00–00, doi:10.1080/02786826.2015.1047012.

Lu, Z., D. G. Streets, E. Winijkul, F. Yan, Y. Chen, T. C. Bond, Y. Feng, M. K. Dubey, S. Liu, J. P. Pinto, and G. R. Carmichael (2015), Light absorption properties and radiative effects of primary organic aerosol emissions, *Environ. Sci. Technol.*, *49*(8), 4868–4877, doi:10.1021/acs.est.5b00211.

Lyyränen, J., J. Jokiniemi, E. I. Kauppinen, and J. Joutsensaari (1999), Aerosol characterisation in medium-speed diesel engines operating with heavy fuel oils, *J. Aerosol Sci.*, *30*(6), 771–784, doi:10.1016/S0021-8502(98)00763-0.

Marelle, L., J. L. Thomas, J.-C. Raut, K. S. Law, J.-P. Jalkanen, L. Johansson, A. Roiger, H. Schlager, J. Kim, A. Reiter, et al. (2016), Air quality and radiative impacts of arctic shipping emissions in the summertime in northern norway: From the local to the regional scale, *Atmos. Chem. Phys.*, *16*(4), 2359–2379, doi:10.5194/acp-16-2359-2016.

Massabò, D., V. Bernardoni, M. Bove, A. Brunengo, E. Cuccia, A. Piazzalunga, P. Prati, G. Valli, and R. Vecchi (2013), A multi-wavelength optical set-up for the characterization of carbonaceous particulate matter, *J. Aerosol Sci.*, *60*, 34–46, doi:10.1016/j.

jaerosci.2013.02.006.

Massabò, D., L. Caponi, V. Bernardoni, M. Bove, P. Brotto, G. Calzolai, F. Cassola, M. Chiari, M. Fedi, P. Fermo, M. Giannoni, F. Lucarelli, S. Nava, A. Piazzalunga, G. Valli, R. Vecchi, and P. Prati (2015), Multi-wavelength optical determination of black and brown carbon in atmospheric aerosols, *Atmos. Environ.*, *108*, 1–12, doi: 10.1016/j.atmosenv.2015.02.058.

Moteki, N., and Y. Kondo (2007), Effects of mixing state on black carbon measurements by laser-induced incandescence, *Aerosol Sci. Technol.*, *41*(4), 398–417, doi: 10.1080/02786820701199728.

Moteki, N., Y. Kondo, and S. Nakamura (2010), Method to measure refractive indices of small nonspherical particles: Application to black carbon particles, *J. Aerosol Sci.*, *41*(5), 513–521, doi:10.1016/j.jaerosci.2010.02.013.

Mueller, L., G. Jakobi, H. Czech, B. Stengel, J. Orasche, J. M. Arteaga-Salas, E. Karg, M. Elsasser, O. Sippula, T. Streibel, J. G. Slowik, A. S. H. Prévôt, J. Jokiniemi, R. Rabe, H. Harndorf, B. Michalke, J. Schnelle-Kreis, and R. Zimmermann (2015), Characteristics and temporal evolution of particulate emissions from a ship diesel engine, *Appl. Energy*, *155*, 204–217, doi:10.1016/j.apenergy.2015.05.115.

Mullins, O. C. (2010), The modified yen model, *Energy & Fuels*, *24*(4), 2179–2207, doi: 10.1021/ef900975e.

Oeder, S., T. Kanashova, O. Sippula, S. C. Sapcariu, T. Streibel, J. M. Arteaga-Salas, J. Passig, M. Dilger, H.-R. Paur, C. Schlager, S. Mülhopt, S. Diabaté, C. Weiss, B. Stengel, R. Rabe, H. Harndorf, T. Torvela, J. Jokiniemi, M.-R. Hirvonen, C. Schmidt-Weber, C. Traidl-Hoffmann, K. A. BéruBé, A. J. Wlodarczyk, Z. Prytherch, B. Michalke, T. Krebs, A. S. H. Prévôt, M. Kelbg, J. Tiggesbäumker, E. Karg, G. Jakobi, S. Scholtes, J. Schnelle-Kreis, J. Lintelmann, G. Matuschek, M. Sklorz, S. Klingbeil, J. Orasche, P. Richthammer, L. Müller, M. Elsasser, A. Reda, T. Gröger, B. Weggler, T. Schwemer, H. Czech, C. P. Rüger, G. Abbaszade, C. Radischat, K. Hiller, J. T. M. Buters, G. Dittmar, and R. Zimmermann (2015), Particulate matter from both heavy fuel oil and diesel fuel shipping emissions show strong biological effects on human lung cells at realistic and comparable in vitro exposure conditions, *PLoS One*, *10*(6), e0126,536, doi:10.1371/journal.pone.0126536.

Onasch, T. B., P. Massoli, P. L. Kebabian, F. B. Hills, F. W. Bacon, and A. Freedman (2015), Single scattering albedo monitor for airborne particulates, *Aerosol Sci. Technol.*, *49*(4), 267–279, doi:10.1080/02786826.2015.1022248.

Petzold, A., J. Ogren, M. Fiebig, P. Laj, S.-M. Li, U. Baltensperger, T. Holzer-Popp, S. Kinne, G. Pappalardo, N. Sugimoto, C. Wehrli, A. Wiedensohler, and X.-Y. Zhang (2013), Recommendations for the interpretation of "black carbon" measurements, *Atmos. Chem. Phys.*, *13*(16), 8365–8379, doi:10.5194/acp-13-8365-2013.

Pokhrel, R. P., E. R. Beamesderfer, N. L. Wagner, J. M. Langridge, D. A. Lack, T. Jayarathne, E. A. Stone, C. E. Stockwell, R. J. Yokelson, and S. M. Murphy (2017), Relative importance of black carbon, brown carbon, and absorption enhancement from clear coatings in biomass burning emissions, *Atmos. Chem. Phys.*, *17*(8), 5063–5078, doi:

10.5194/acp-17-5063-2017.

Popovicheva, O., E. Kireeva, N. Shonija, N. Zubareva, N. Persiantseva, V. Tishkova, B. Demirdjian, J. Moldanová, and V. Mogilnikov (2009), Ship particulate pollutants: Characterization in terms of environmental implication, *J. Environ. Monit.*, *11*(11), 2077–2086, doi:10.1039/B908180A.

Price, D. J., C.-L. Chen, L. M. Russell, M. A. Lamjiri, R. Betha, K. Sanchez, J. Liu, A. K. Y. Lee, and D. R. Cocker (2016), More unsaturated, cooking-type hydrocarbon-like organic aerosol particle emissions from renewable diesel compared to ultra low sulfur diesel in at-sea operations of a research vessel, *Aerosol Science and Technology*, *51*(2), 135–146, doi:10.1080/02786826.2016.1238033.

Rüger, C. P., M. Sklorz, T. Schwemer, and R. Zimmermann (2015), Characterisation of ship diesel primary particulate matter at the molecular level by means of ultra-high-resolution mass spectrometry coupled to laser desorption ionisation—comparison of feed fuel, filter extracts and direct particle measurements, *Anal. Bioanal.Chem.*, *407*(20), 5923–5937, doi:10.1007/s00216-014-8408-1.

Saleh, R., P. J. Adams, N. M. Donahue, and A. L. Robinson (2016), The interplay between assumed morphology and the direct radiative effect of light-absorbing organic aerosol, *Geophys. Res. Lett.*, *43*(16), 8735–8743, doi:10.1002/2016gl069786.

Sandradewi, J., A. S. Prévôt, S. Szidat, N. Perron, M. R. Alfarra, V. A. Lanz, E. Weingartner, and U. Baltensperger (2008), Using aerosol light absorption measurements for the quantitative determination of wood burning and traffic emission contributions to particulate matter, *Environ. Sci. Technol.*, *42*(9), 3316–3323, doi:10.1021/es702253m.

Schwarz, J. P., R. S. Gao, D. W. Fahey, D. S. Thomson, L. A. Watts, J. C. Wilson, J. M. Reeves, M. Darbeheshti, D. G. Baumgardner, G. L. Kok, S. H. Chung, M. Schulz, J. Hendricks, A. Lauer, B. Kärcher, J. G. Slowik, K. H. Rosenlof, T. L. Thompson, A. O. Langford, M. Loewenstein, and K. C. Aikin (2006), Single-particle measurements of midlatitude black carbon and light-scattering aerosols from the boundary layer to the lower stratosphere, *J. Geophys. Res.*, *111*, D16,207, doi:10.1029/2006JD007076.

Schwarz, J. P., R. S. Gao, J. R. Spackman, L. A. Watts, D. S. Thomson, D. W. Fahey, T. B. Ryerson, J. Peischl, J. S. Holloway, M. Trainer, G. J. Frost, T. Baynard, D. A. Lack, J. A. de Gouw, C. Warneke, and L. A. D. Negro (2008), Measurement of the mixing state, mass, and optical size of individual black carbon particles in urban and biomass burning emissions, *Geophys. Res. Lett.*, *35*(13), doi:10.1029/2008gl033968.

Sedlacek, A. J., E. R. Lewis, T. B. Onasch, A. T. Lambe, and P. Davidovits (2015), Investigation of refractory black carbon-containing particle morphologies using the single-particle soot photometer (SP2), *Aerosol Science and Technology*, *49*(10), 872–885, doi:10.1080/02786826.2015.1074978.

Seinfeld, J. H., and S. N. Pandis (2012), *Atmospheric chemistry and physics: from air pollution to climate change*, John Wiley & Sons.

Sippula, O., B. Stengel, M. Sklorz, T. Streibel, R. Rabe, J. Orasche, J. Lintelmann, B. Michalke, G. Abbaszade, C. Radischat, T. M. Grüger, J. Schnelle-Kreis, H. Harndorf, and R. Zimmermann (2014), Particle emissions from a marine engine: Chemical

composition and aromatic emission profiles under various operating conditions, *Environ. Sci. Technol.*, *48*, 11,721–11,729, doi:10.1021/es502484z, pMID: 25202837.

Slowik, J. G., E. S. Cross, J.-H. Han, P. Davidovits, T. B. Onasch, J. T. Jayne, L. R. Williams, M. R. Canagaratna, D. R. Worsnop, T. K. Chakrabarty, J. Moosmüller, E. P. Arnott, J. P. Schwarz, R.-S. Gao, F. W. Fahey, G. L. Kok, and A. Petzold (2007), An inter-comparison of instruments measuring black carbon content of soot particles, *Aerosol Sci. Technol.*, *41*(3), 295–314, doi:10.1080/02786820701197078.

Sorensen, C. (2001), Light scattering by fractal aggregates: a review, *Aerosol Sci. Technol.*, *35*(2), 648–687, doi:10.1080/02786820117868.

Sorensen, C. (2011), The mobility of fractal aggregates: a review, *Aerosol Sci. Technol.*, *45*(7), 765–779, doi:10.1080/02786826.2011.560909.

Stephens, M., N. Turner, and J. Sandberg (2003), Particle identification by laser-induced incandescence in a solid-state laser cavity, *Appl. Opt.*, *42*(19), 3726–3736, doi:10.1364/AO.42.003726.

Stout, S., and Z. Wang (2016), *Standard Handbook Oil Spill Environmental Forensics: Fingerprinting and Source Identification*, 641–683 pp., Academic Press.

Streibel, T., J. Schnelle-Kreis, H. Czech, H. Harndorf, G. Jakobi, J. Jokiniemi, E. Karg, J. Lintelmann, G. Matuschek, B. Michalke, L. Müller, J. Orasche, J. Passig, C. Radischat, R. Rabe, R. Ahmed, C. Rüger, T. Schwemer, O. Sippula, B. Stengel, M. Sklorz, T. Torvela, B. Weggler, and R. Zimmermann (2017), Aerosol emissions of a ship diesel engine operated with diesel fuel or heavy fuel oil, *Environmental Science and Pollution Research*, p. 10976, doi:10.1007/s11356-016-6724-z.

Taylor, J., J. Allan, D. Liu, M. Flynn, R. Weber, X. Zhang, B. Lefer, N. Grossberg, J. Flynn, and H. Coe (2015), Assessment of the sensitivity of core/shell parameters derived using the single-particle soot photometer to density and refractive index, *Atmos. Meas. Tech.*, *8*(4), 1701–1718, doi:10.5194/amt-8-1701-2015.

Unger, N., T. C. Bond, J. S. Wang, D. M. Koch, S. Menon, D. T. Shindell, and S. Bauer (2010), Attribution of climate forcing to economic sectors, *P. Patl. Acad. Sci. USA*, *107*(8), 3382–3387, doi:10.1073/pnas.0906548107.

Wang, Q., R.-J. Huang, Z. Zhao, J. Cao, H. Ni, X. Tie, S. Zhao, X. Su, Y. Han, Z. Shen, Y. Wang, N. Zhang, Y. Zhou, and J. C. Corbin (2016), Physicochemical characteristics of black carbon aerosol and its radiative impact in a polluted urban area of china, *J. Geophys. Res.-Atmos.*, *121*(20), 12,505–12,519, doi:10.1002/2016jd024748.

Wu, Y., X. Wang, J. Tao, R. Huang, P. Tian, J. Cao, L. Zhang, K.-F. Ho, Z. Han, and R. Zhang (2017), Size distribution and source of black carbon aerosol in urban beijing during winter haze episodes, *Atmospheric Chemistry and Physics*, *17*(12), 7965–7975, doi:10.5194/acp-17-7965-2017.

Yuan, J.-F., X.-F. Huang, L.-M. Cao, J. Cui, Q. Zhu, C.-N. Huang, Z.-J. Lan, and L.-Y. He (2016), Light absorption of brown carbon aerosol in the prd region of china, *Atmos. Chem. Phys.*, *16*(3), 1433–1443, doi:10.5194/acp-16-1433-2016.

Zieger, P., O. Väisänen, J. C. Corbin, D. G. Partridge, S. Bastelberger, M. Mousavi-Fard, B. Rosati, M. Gysel, U. K. Krieger, C. Leck, A. Nenes, I. Riipinen, A. Virtanen, and

M. E. Salter (2017), Revising the hygroscopicity of inorganic sea salt particles, *Nat. Commun.*, (15883), doi:10.1038/ncomms15883.

Zimmerman, N., C.-H. Jeong, J. M. Wang, M. Ramos, J. S. Wallace, and G. J. Evans (2015), A source-independent empirical correction procedure for the fast mobility and engine exhaust particle sizers, *Atmos. Environ.*, *100*, 178–184, doi:dx.doi.org/10.1016/j.atmosenv.2014.10.054.

Zotter, P., H. Herich, M. Gysel, I. El-Haddad, Y. Zhang, G. Močnik, C. Hüglin, U. Baltensperger, S. Szidat, and A. S. H. Prévôt (2017), Evaluation of the absorption ångström exponents for traffic and wood burning in the aethalometer-based source apportionment using radiocarbon measurements of ambient aerosol, *Atmos. Chem. Phys.*, *17*(6), 4229–4249, doi:10.5194/acp-17-4229-2017.

F1.

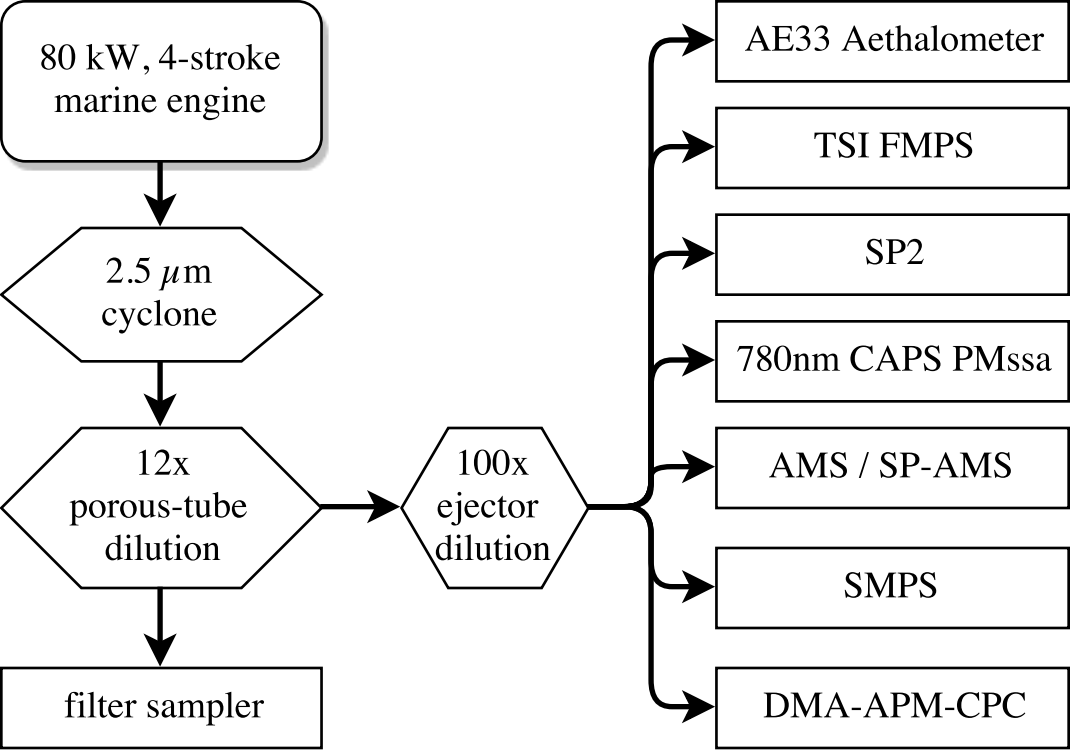
80 kW, 4-stroke marine engine
2.5 μm cyclone
12x porous-tube dilution
filter sampler
100x ejector dilution
AE33 Aethalometer
TSI FMPS
SP2
780nm CAPS PMssa
AMS / SP-AMS
SMPS
DMA-APM-CPC

F2.

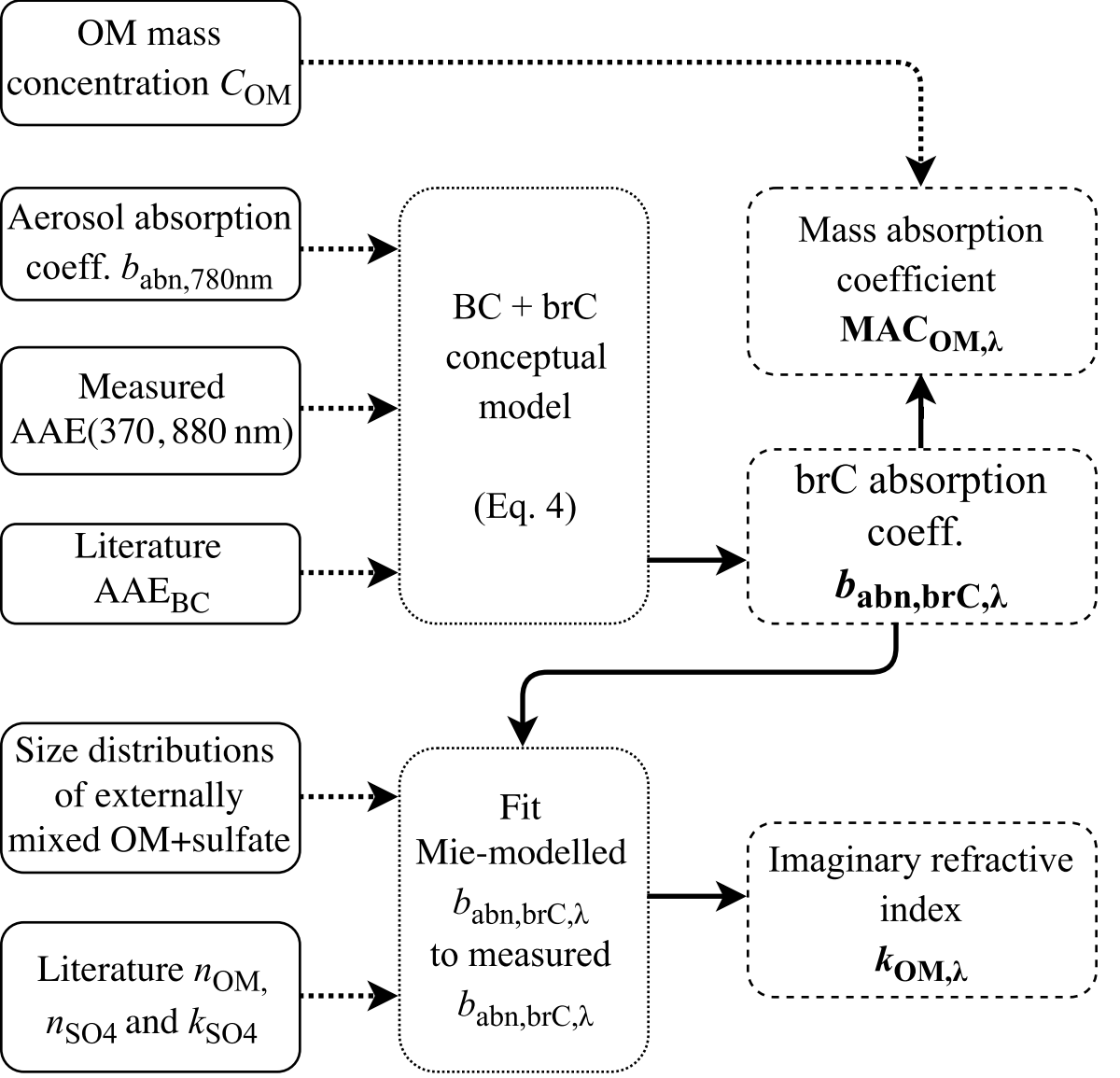
OM mass concentration C_{OM}
Aerosol absorption coeff. $b_{abn,780nm}$
Measured AAE(370, 880 nm)
Literature AAE_{BC}
BC + brC conceptual model
(Eq. 4)
Mass absorption coefficient $\mathbf{MAC_{OM,\lambda}}$
brC absorption coeff. $\boldsymbol{b_{abn,brC,\lambda}}$
Size distributions of externally mixed OM+sulfate
Literature n_{OM}, n_{SO4} and k_{SO4}
Fit Mie-modelled $b_{abn,brC,\lambda}$ to measured $b_{abn,brC,\lambda}$
Imaginary refractive index $\boldsymbol{k_{OM,\lambda}}$

F3.

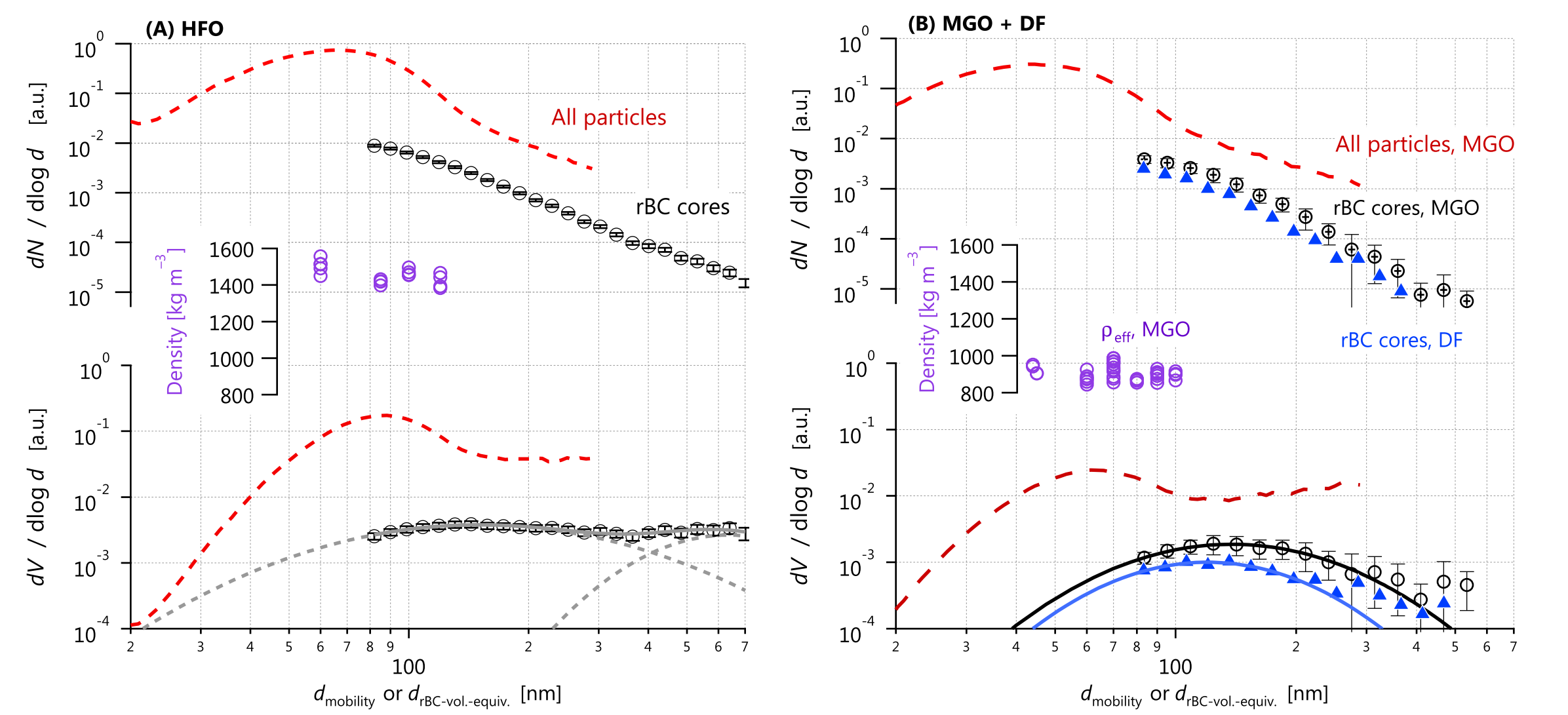
(A) HFO
(B) MGO + DF
All particles
rBC cores
All particles, MGO
rBC cores, MGO
rBC cores, DF
ρeff, MGO
Density [kg m−3]
dN / dlog d [a.u.]
dV / dlog d [a.u.]
dmobility or drBC-vol.-equiv. [nm]

F4.

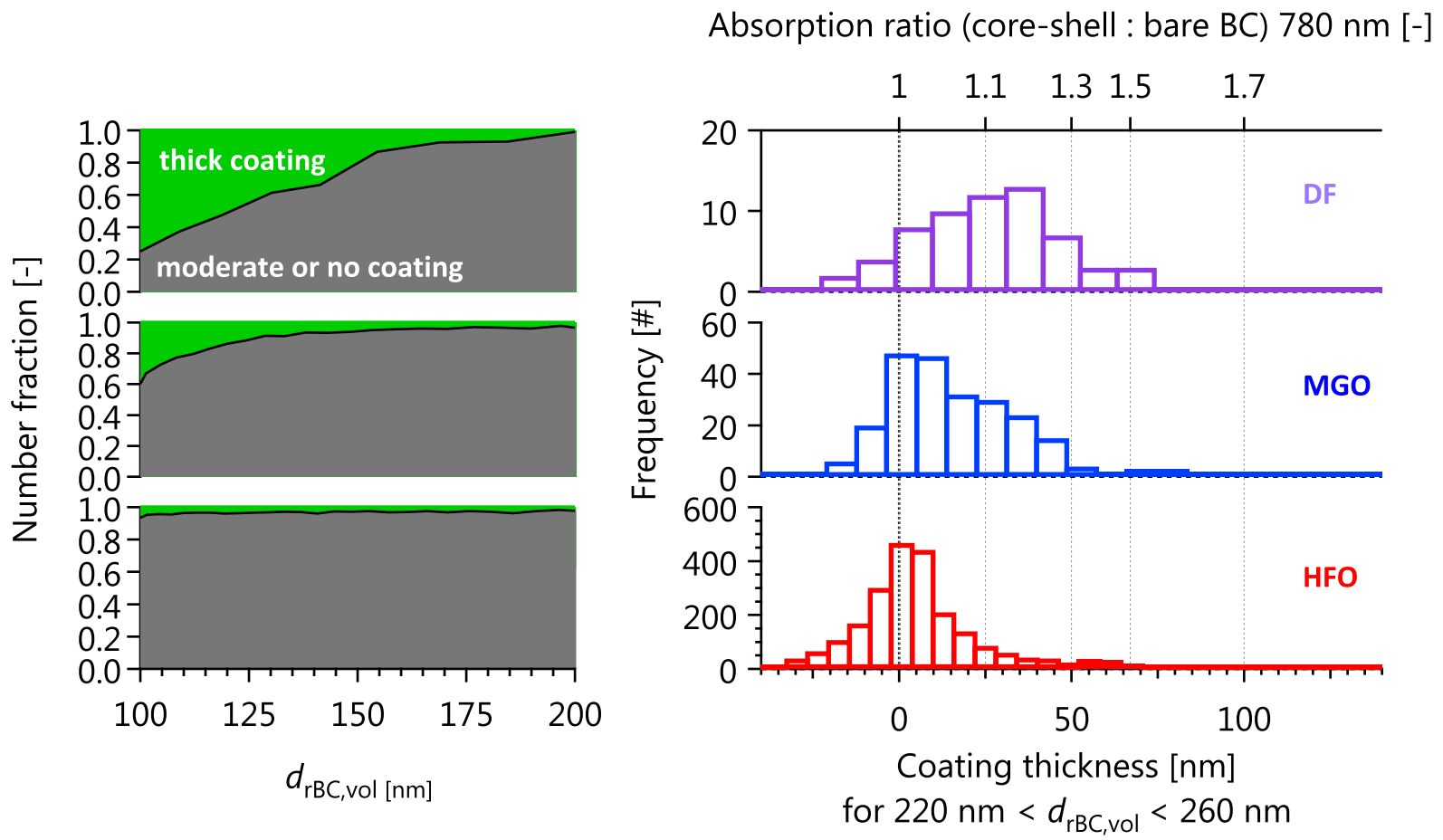
thick coating
moderate or no coating
Number fraction [-]
1.0
0.8
0.6
0.4
0.2
0.0
100
125
150
175
200
$d_{rBC,vol}$ [nm]
Absorption ratio (core-shell : bare BC) 780 nm [-]
1
1.1
1.3
1.5
1.7
Frequency [#]
20
10
0
DF
60
40
20
0
MGO
600
400
200
0
HFO
0
50
100
Coating thickness [nm]
for 220 nm < $d_{rBC,vol}$ < 260 nm

F5.

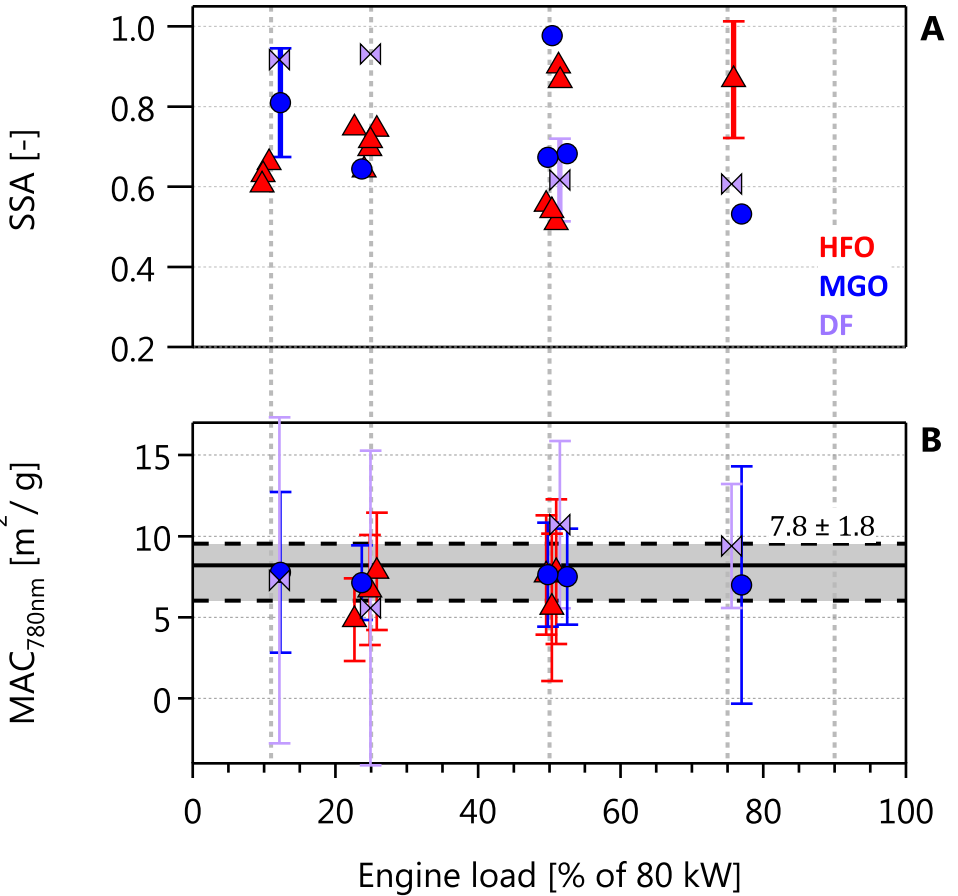
A
B
SSA [-]
1.0
0.8
0.6
0.4
0.2
HFO
MGO
DF
MAC780nm [m2 / g]
15
10
5
0
7.8 ± 1.8
0
20
40
60
80
100
Engine load [% of 80 kW]

F6.

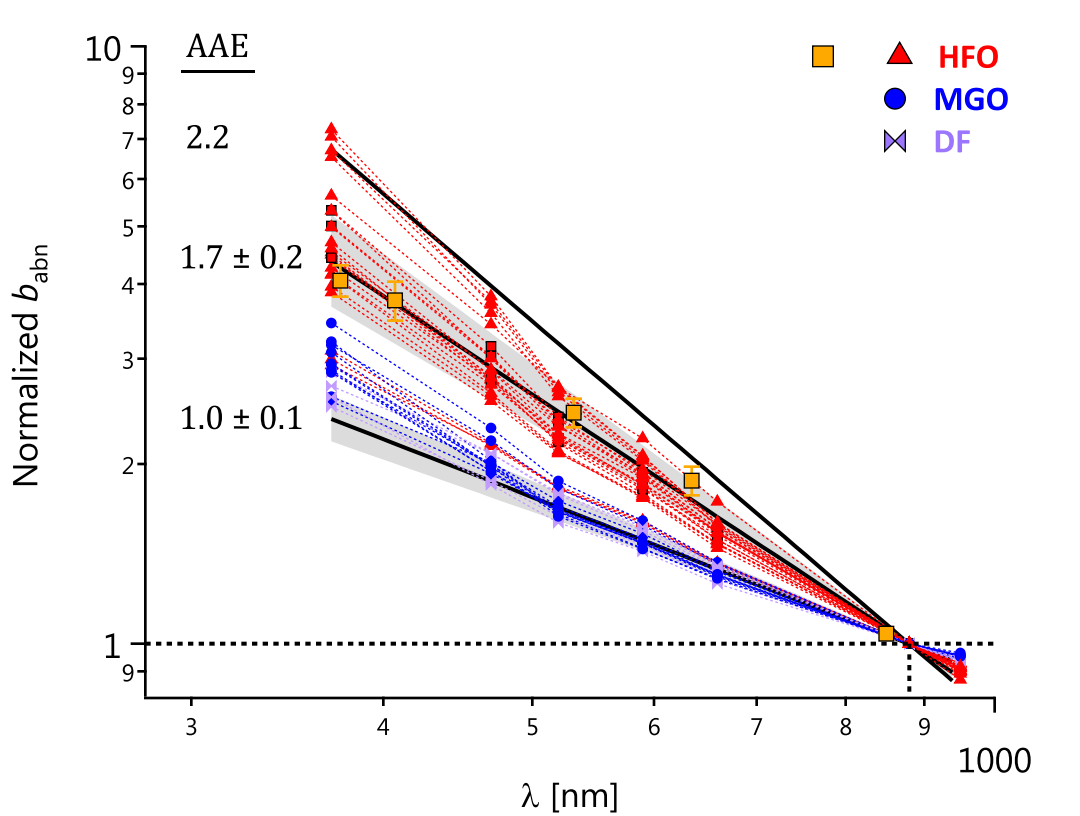
AAE
2.2
1.7 ± 0.2
1.0 ± 0.1
HFO
MGO
DF
Normalized b_{abn}
λ [nm]
10
9
8
7
6
5
4
3
2
1
9
3
4
5
6
7
8
9
1000

F7.

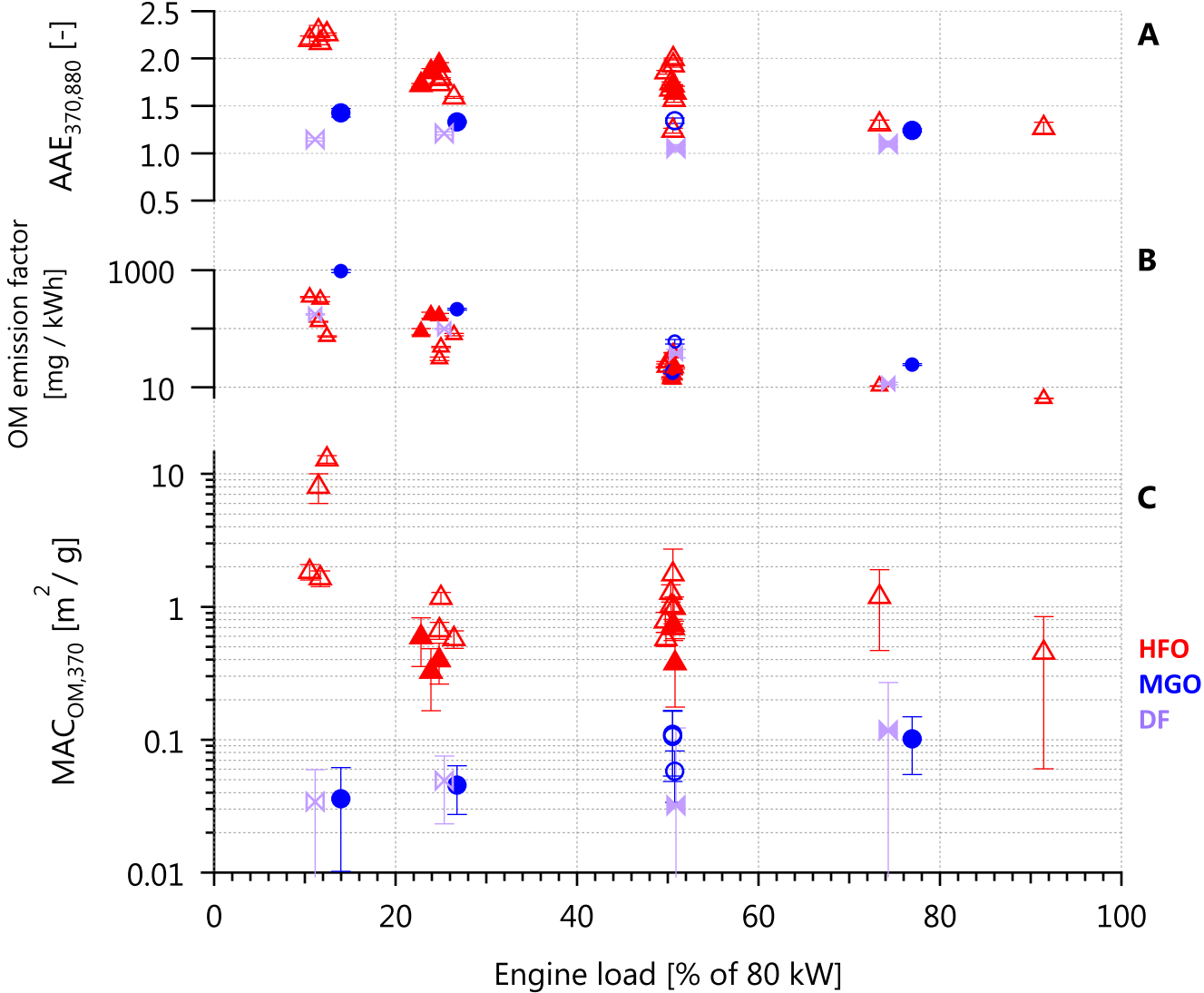
A
B
C
OM emission factor [mg / kWh]
AAE370,880 [-]
MAC OM,370 [m2 / g]
2.5
2.0
1.5
1.0
0.5
1000
10
10
1
0.1
0.01
0
20
40
60
80
100
Engine load [% of 80 kW]
HFO
MGO
DF

F8.

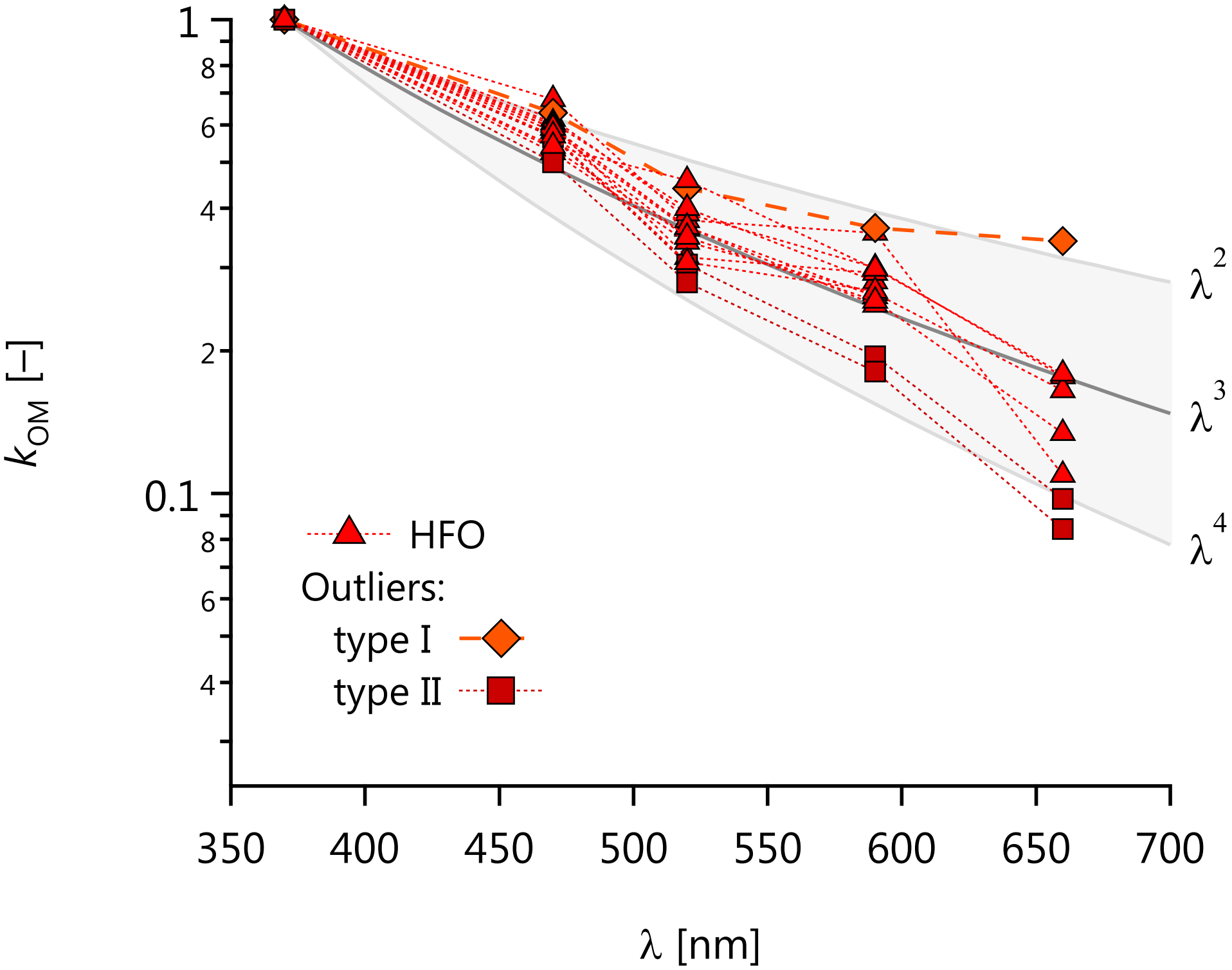
1
8
6
4
2
0.1
8
6
4
k_{OM} [–]
HFO
Outliers:
type I
type II
λ^2
λ^3
λ^4
350
400
450
500
550
600
650
700
λ [nm]

F9.

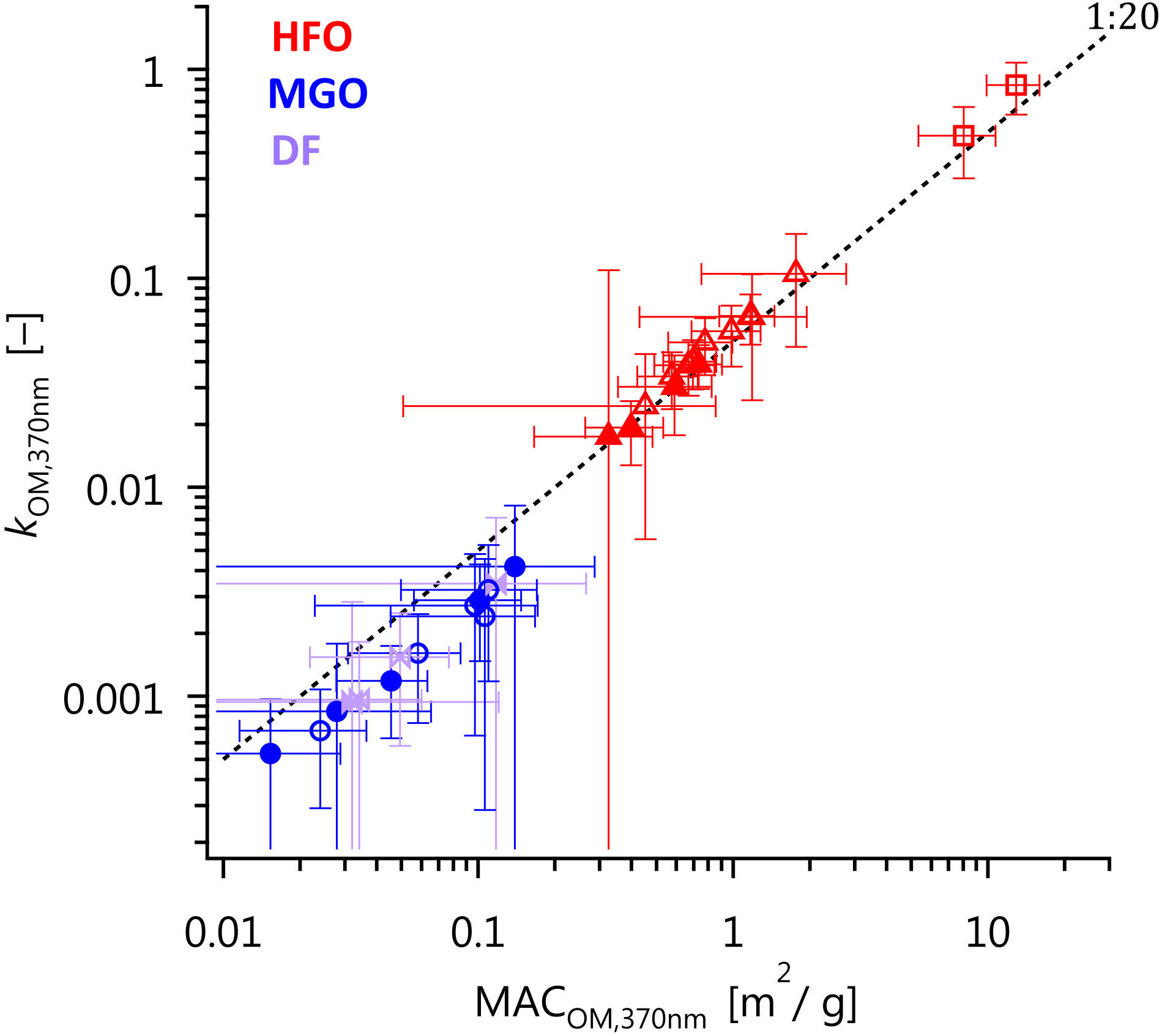
HFO
MGO
DF
1:20
1
0.1
0.01
0.001
$k_{OM,370nm}$ [–]
0.01
0.1
1
10
$MAC_{OM,370nm}$ [m^2 / g]

F10.

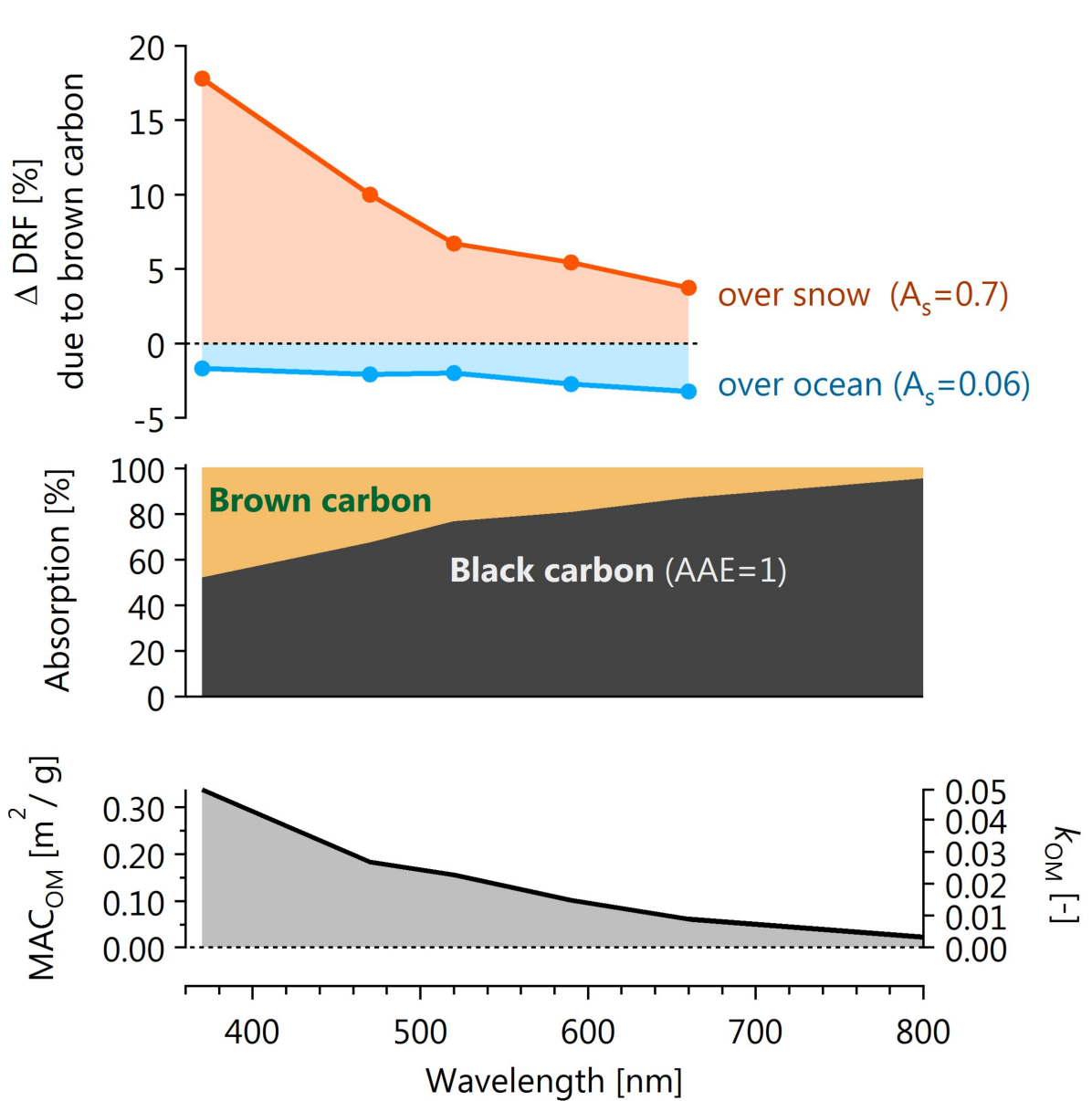
Δ DRF [%]
due to brown carbon
20
15
10
5
0
-5
over snow (A_s=0.7)
over ocean (A_s=0.06)
Absorption [%]
100
80
60
40
20
0
Brown carbon
Black carbon (AAE=1)
MAC_OM [m^2 / g]
0.30
0.20
0.10
0.00
k_OM [-]
0.05
0.04
0.03
0.02
0.01
0.00
400
500
600
700
800
Wavelength [nm]